Aitken Mode Aerosols Buffer Decoupled Mid-latitude Boundary Layer Clouds Against Precipitation Depletion

Isabel L. McCoy[1,2,3,4], Matthew C. Wyant[1], Peter N. Blossey[1], Christopher S. Bretherton[5], and Robert Wood[1]

[1]Department of Atmospheric Sciences, University of Washington, Seattle, WA, USA
[2]Cooperative Programs for the Advancement of Earth System Science, University Corporation for Atmospheric Research, Boulder, CO, USA
[3]Cooperative Institute for Research in Environmental Sciences, University of Colorado, Boulder, CO, USA
[4]National Oceanic and Atmospheric Administration, Chemical Sciences Laboratory, Boulder, CO, USA
[5]Allen Institute for Artificial Intelligence, Seattle, WA, USA

Key Points:

- Observations of mid-latitude decoupled low clouds constrain a large-eddy simulation investigating aerosol-cloud-precipitation interactions
- Boundary layer Aitken activation and turbulent and convective fluxes restore accumulation mode aerosols against precipitation losses
- Large-scale ascent moistens and brightens clouds while Aitken buffering acts to sustain brighter, more homogeneous clouds

Corresponding author: Isabel L. McCoy, isabel.mccoy@noaa.gov

Abstract

Aerosol-cloud-precipitation interactions are a leading source of uncertainty in estimating climate sensitivity. Remote marine boundary layers where accumulation mode (∼100-400 nm diameter) aerosol concentrations are relatively low are very susceptible to aerosol changes. These regions also experience heightened Aitken mode aerosol (∼10-100 nm) concentrations associated with ocean biology. Aitken aerosols may significantly influence cloud properties and evolution by replenishing cloud condensation nuclei and droplet number lost through precipitation (i.e., Aitken buffering). We use a large-eddy simulation with an Aitken-mode enabled microphysics scheme to examine the role of Aitken buffering in a mid-latitude decoupled boundary layer cloud regime observed on July 15, 2017 during the ACE-ENA flight campaign: cumulus rising into stratocumulus under elevated Aitken concentrations (∼100-200 mg^{-1}). *In situ* measurements are used to constrain and evaluate this case study. Our simulation accurately captures observed aerosol-cloud-precipitation interactions and reveals time-evolving processes driving regime development and evolution. Aitken activation into the accumulation mode occurs primarily in the cumulus layer, providing a reservoir for turbulence and convection to carry accumulation aerosols into the drizzling stratocumulus layer above. Thus, the cloud regime is buffered against precipitation removal, reducing cloud break-up and associated increases in heterogeneity. We examine cloud evolution sensitivity to initial aerosol conditions. With halved accumulation number, Aitken aerosols restore accumulation concentrations, maintain droplet number similar to original values, and prevent cloud break-up. Without Aitken aerosols, precipitation-driven cloud break-up occurs rapidly. In this regime, mesoscale and synoptic-scale uplift enhance cloud condensate and brightness, but Aitken buffering sustains brighter, more homogeneous clouds for longer.

Plain Language Summary

Aerosols, small particles in the atmosphere associated with ocean biology, sea spray, land, and human-produced emissions, influence cloud brightness and, by suppressing precipitation and subsequent break up, cloud lifetime. Understanding aerosol-cloud-precipitation interactions is critical in understanding how aerosols influence the climate system. This study examines how the very smallest aerosol particles modify cloud formation, brightness, and lifetime over the North Atlantic ocean. We utilize a recent set of aircraft and satellite observations from a dedicated field campaign as well as a detailed model that resolves fine-scale interactions important to cloud development. After comparing the model to real-world observations, we test how modifying the amount of small particles impacts the cloud brightness and lifetime. We find that the small particles are able to offset precipitation removal of larger particles, helping clouds to last longer and stay brighter.

1 Introduction

Recently, aerosol-cloud interaction (aci) in liquid clouds has been identified as a key, remaining source of uncertainty in accurately estimating climate sensitivity (Bellouin et al., 2020). Aci impacts the climate system in two ways (Boucher, 2013; Bellouin et al., 2020; Christensen et al., 2022). The first is through radiative forcing (RF_{aci}), which manifests as a change in cloud droplet number concentration (N_d) in response to a change in aerosol while other macrophysical characteristics (e.g., liquid water content) remain constant (Twomey, 1977): increasing aerosol amount leads to increasing N_d and an increase in the fraction of shortwave reflected back to space (i.e., albedo) associated with the accompanying reduction in surface area per droplet. The second is through cloud adjustments, which manifest as a change in cloud macrophysical characteristics (e.g., cloud liquid, amount, thickness, etc.) through changes in cloud microphysics (e.g., precipitation, evaporation, etc.) (Albrecht, 1989). These combined effects in response to a change

in aerosol (i.e., from the pre-industrial aerosol state to the present day) are known as the effective radiative forcing (ERF_{aci}).

Global climate models (GCMs) have particular difficulty in capturing aci in cloud regimes that are biologically active with little anthropogenic influence (e.g., Carslaw et al., 2013; McCoy et al., 2020). Some of this is likely due to incomplete representation of Aitken aerosol production and its contribution to aci (Gordon et al., 2017; McCoy et al., 2021). Aitken aerosols (∼10-100 nm in diameter) form through various processes including gas to particle conversion from ocean biology emissions (Seinfeld & Pandis, 2016) which can occur at cloud edges (e.g., Clarke et al., 1998; Kazil et al., 2011), continental anthropogenic emissions (e.g., Twohy et al., 2002), and, in recent studies, from sea spray production (Lawler et al., 2021; Xu et al., 2022). They have been observed in high concentrations in the free troposphere (FT) intermittently across the globe (Williamson et al., 2019). In the boundary layer, where they are sometimes generated (Zheng et al., 2021), Aitken particles act as a key source of accumulation mode aerosol (∼100-400 nm) (e.g., Covert et al., 1996; Sanchez et al., 2018). Accumulation mode aerosols are then activated in moist updrafts into cloud condensation nuclei (CCN). Enhanced supersaturation (Kaufman & Tanré, 1994) and updraft strength (Pöhlker et al., 2021), particularly in the absence of accumulation mode particles, can facilitate activation of smaller, Aitken particles into CCN as well (Fan et al., 2018).

Aitken mode-aerosols may have an additional role to play in aerosol-cloud-precipitation interactions. Drawing on Southern Ocean observations, McCoy et al. (2021) recently hypothesized that Aitken particles buffer precipitating boundary layer clouds against cloud droplet depletion: as precipitation removes accumulation mode aerosol, peak supersaturation increases in updrafts, and larger aerosols in the Aitken mode are able to activate and grow to CCN, restoring N_d. This buffering mechanism is consistent with the idea that changes in cloud-active aerosol can be partially compensated when changes in aerosol composition and size distributions lead to increased supersaturation and thus increased activation of smaller condensation nuclei (e.g., 'microphysical buffering', Stevens & Feingold, 2009; Twomey, 1959). During the biologically-active Southern Ocean Austral summer, Aitken aerosol are plentiful both in a substantial FT reservoir developed through synoptic-scale uplift and in the boundary layer (BL) as a result of synoptic-scale descent (Covert et al., 1996; McCoy et al., 2021). Southern Ocean clouds have been observed to have many fewer optically-thin cloud features than in similar clouds observed in the Northeast Pacific Stratocumulus (Sc) to Cumulus (Cu) transitions (O, Wood, & Tseng, 2018; McCoy et al., 2021). In the sub-tropics, these features are generated in association with precipitation-driven depletion of the cloud droplet and accumulation mode aerosol populations (Wood et al., 2018; O, Wood, & Bretherton, 2018; O, Wood, & Tseng, 2018). Less frequent occurrence of optically-thin cloud features in the Southern Ocean is consistent with a damping of precipitation processes by Aitken-buffering.

Recent large-eddy simulation (LES) and observational studies have found Aitken aerosols impact cloud microphysical and radiative properties in pristine environments (Pöhlker et al., 2021; Wyant et al., 2022), although their influence is modulated by cloud phase (Bulatovic et al., 2021). In particular, Wyant et al. (2022, hereafter W22) developed an Aitken-mode enabled microphysics scheme that predicts time evolution of aerosol-cloud-precipitation interactions by including aerosol sinks and sources (albeit neglecting new particle formation). W22 utilized an idealized Southeast Pacific case study of deep, precipitating Sc informed by *in situ* observations to directly evaluate the Aitken-buffering hypothesis. They simulated this case over several days, finding a gradual loss of accumulation mode aerosol to drizzle formation led to a transition to an ultra-clean, low cloud fraction, strongly precipitating Cu state. This transition could be delayed by increasing Aitken concentrations above the inversion or through fluxes from the surface.

The Aitken-buffering mechanism, which has both observational (McCoy et al., 2021) and modeling (Wyant et al., 2022) support, has important implications for our under-

standing of aci and past and future climates. Konsta et al. (2022) recently found that the "too few, too bright" bias in GCMs has persisted in many state-of-the-art models largely due to GCMs' difficulty in capturing the heterogeneity of clouds at lower cloud fractions. Specifically, GCMs fail to represent the wide-spread occurrence of optically-thin cloud features (Konsta et al., 2022) that occur across a variety of mesoscale cloud morphology patterns (Leahy et al., 2012; O, Wood, & Tseng, 2018; Mieslinger et al., 2021; McCoy et al., 2023) and may depend in part on the absence of Aitken aerosols (McCoy et al., 2021). Variations in optically-thin cloud amount across morphology patterns contributes to differences in their cloud radiative impact and how we expect them to feed back on the climate system under climate change (McCoy et al., 2023). Incomplete representation of Aitken aerosol processes in GCMs may also influence our estimation of RF_{aci} and therefore ERF_{aci} as Aitken aerosols may play a critical role in regulating N_d in pristine, pre-industrial environments (Gordon et al., 2017, 2016; McCoy et al., 2020). Thus, identifying the key processes involved in aerosol-cloud-precipitation interactions driven by Aitken aerosols and understanding their nuances has utility in improving both our knowledge of the climate system and the representation of cloud-aerosol interactions in models used for climate prediction.

In this study, we build on the work of W22 by utilizing their Aitken-enabled microphysics scheme in large eddy simulations (Section 2.2) to examine the influence of Aitken aerosols on an observationally-constrained case study sampled during the recent ACE-ENA (Aerosol and Cloud Experiments in the Eastern North Atlantic) flight campaign in the Northeast Atlantic (Wang et al., 2022). Specifically, we examine a case of Cu rising into Sc under substantial Aitken aerosol concentrations that was sampled by aircraft on July 15, 2017. We extend W22 by using these *in situ* observations (Section 2.1) to constrain the LES control simulation (Section 3.1). Successful simulation of this case allows us to identify the key processes involved in the evolution of clouds in such a regime (Section 3.2). Aerosol sensitivity studies are conducted (Section 4) to examine the dependence on initial aerosol state and subsequent nuances of rapid aerosol processing, changes in cloud microphysics, radiative properties, and heterogeneity (as measured by the development of optically-thin cloud features). We especially focus on the influence of Aitken aerosols on cloud properties under this meteorologically-forced regime. We conclude with a discussion (Section 5) and summary (Section 6).

2 Data and Methods

2.1 Observations for the ACE-ENA Case Study

In situ observations from the July 15, 2017 flight (Figure 1) during the summer phase of the ACE-ENA campaign (Wang et al., 2022) form the basis for our LES case study. This research flight by the Department of Energy G-1 aircraft (hereafter RF16 of the campaign) sampled a system of Cu (bases at ∼500m) rising into Sc (∼1000-1500m) to the northwest of Graciosa Island (Figure 1). This system gradually advected to the southwest over the day (e.g., Figure 2a, Wang et al., 2022). The G-1 aircraft utilized a Lagrangian-drift sampling pattern consisting of multiple stacked level legs ∼60 km in length. Each leg followed a straight, crosswind line at altitudes set to sample above, in, and below cloud and ended in a vertical ascent profile to the next level leg altitude (Figure 1b). ERA5 reanalysis extracted for the ACE-ENA campaign region show that, over the course of the day, the atmosphere experienced increasing large-scale uplift (Figure S3a) and an associated cooling and moistening by large-scale vertical advection (Figure S3b, c). Mesoscale moisture convergence (e.g., Bretherton & Blossey, 2017) can be encouraged by large-scale uplift (e.g., as seen in trade-wind clouds Narenpitak et al., 2021), and may contribute to the deepening and moistening of clouds observed in this case.

The G-1 aircraft was outfitted with a suite of instruments, a subset of which we utilize to both develop and compare with our LES case study. The Fast Integrated Mo-

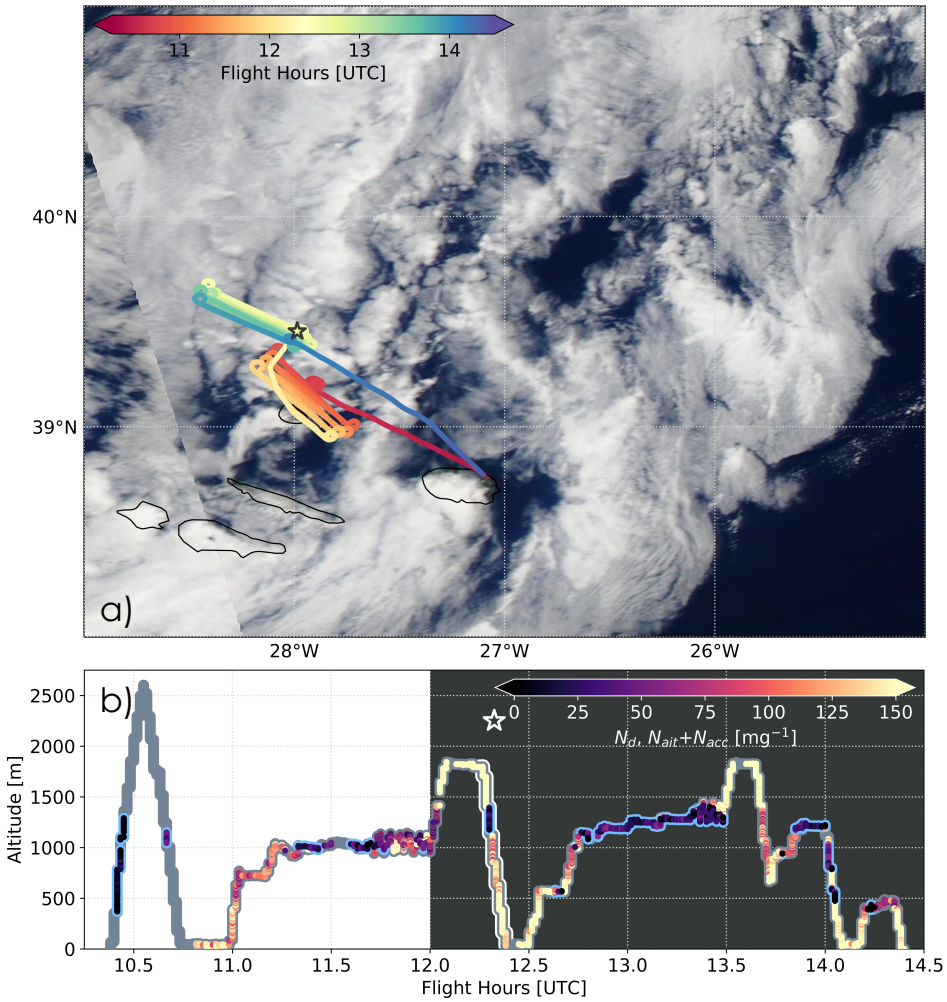

Figure 1. a) MODIS *Aqua* visual imagery for RF16 on July 15, 2017 at 14:30 UTC or 13:30 local time, with ACE-ENA flight path colored by time. b) Flight altitude vs. UTC time (grey) with color overlay of observations (where available) of total aerosol from simultaneously sampled N_{ait}+N_{acc} or, in cloud, N_d. In cloud sampling, where LWC≥0.01 g kg^{-1}, is outlined in blue. The dark gray background from 12-14:30 UTC is the observational comparison period used in model evaluation. Separately plotted N_{ait} and N_{acc} versions are shown in Figure S1. The profile used for initializing aerosol is marked with a star in a), b) and outlined in white in b).

bility Spectrometer (FIMS) and the Passive Cavity Aerosol Spectrometer Probe (PCASP) provide size distributions and number concentrations for Aitken (∼10-100 nm) and Accumulation (∼100-400 nm) mode size ranges, respectively. The FIMS resolves the full 10-400 nm size range while the PCASP resolves the larger, accumulation sizes only (e.g., Figure 4). Total aerosol number concentrations for this study are calculated as the sum of the Aitken and accumulation number concentrations from these specified size ranges, which is found to be similar to the observations from the Condensation Particle Counter (CPC, sizes ≥10 nm, not shown). The Fast Cloud Droplet Probe (FCDP) is used for cloud N_d and liquid water content (LWC). Precipitation flux, which includes cloud droplet sedimentation, is calculated from droplet spectra measurements assuming terminal fall-speeds from Rogers and Yau (1989). Spectra are based on two instruments that optimally sample different drop size ranges (results are not sensitive to the diameter cutoff): the FCDP

(selecting diameters $\leq$50 μm) and the Two-Dimensional Stereo Particle Imaging Probe (2DS, diameters $\geq$50 μm).

For the model-observation comparison, we focus on the second half of the flight period (12-14:30 UTC). Note that local solar time is $\sim$ 2 hours behind UTC. This portion of the flight was cloud-rich and generally moister than the first, drier half (see blue outlines, Figure 1b). Aitken and accumulation aerosol size ranges are more consistently simultaneously sampled in the second half as well (shown separately in Figure S1 and as a sum, when both sampled, in Figure 1b). Comparison levels are selected to be further from clouds where observations are sparse. The profile at $\sim$12:15pm (profile 2, P2) sampled the depth of the boundary layer and is used as the initial LES aerosol profile (star in Figure 1, S1, discussed further in Section 2.2).

We also compare our results against cloud liquid water path, cloud optical depth (τ), and broadband albedo retrievals for the ACE-ENA campaign (ARM Data Center, 2017) from the NASA SATCORPS (Satellite Cloud Observations and Radiative Property retrieval System) product which applies the VISST (Visible Infrared Solar-infrared Split-Window Technique) algorithm to Meteosat-10 satellite channels (Patrick Minnis et al., 2001; Minnis et al., 2008, 2011). The broadband albedo retrieval product includes a correction based on converting to shortwave flux and regionally (5 x 5°) normalizing to Edition 4 of the CERES (Clouds and the Earth's Radiant Energy System) Aqua SSF1deg product for the corresponding month. Model-satellite comparisons are also restricted to 12-14:30 UTC, as for the aircraft comparisons, and LES output is coarsened to the SATCORPS temporal (0.5 hr) and spatial ($\sim$3 km) resolutions. In order to capture a representative sample of this case's cloud heterogeneity while restricted to the coarser satellite resolution, we use a 3 x 3° domain upwind and overlapping the flight region (26-29°W and 39-42°N, Figure 1a, S2). We sub-sample this into 144 sub-domains of comparable area to the LES simulation domain ($\sim$0.25 x 0.25°, see Figure S2b for an example).

2.2 Aitken-aerosol-enabled Large-Eddy Simulations

We utilize W22's novel two-mode aerosol microphysics scheme for the System for Atmospheric Modeling (SAM) LES simulations (25.6 x 25.6 km domain with 100 m resolution). This scheme extends the single-mode two-moment prognostic aerosol scheme of Berner et al. (2013) by including Aitken aerosol evolution and a simple representation of sulfur chemistry. Seven prognostic variables represent accumulation and Aitken log-normal aerosol modes in air and droplets as well as three gas species (H_2SO_4, SO_2, and DMS). Scavenging of interstitial and other unactivated aerosol by cloud and rain drops are treated as in Berner et al. (2013), while coagulation of unactivated aerosols follow Binkowski and Shankar (1995). A simplified scheme for capturing basic influences of sulfur chemistry on model aerosols is also included, but new particle formation (e.g., aerosols nucleating from gas-phase H_2SO_4) is neglected for simplicity (unlike in Kazil et al., 2011). The only sources of Aitken aerosols considered in the scheme are from surface fluxes and entrainment from the FT. Two aerosol modes are used to approximately capture the Aitken ($\sim$10-100 nm) and accumulation ($\sim$100-400 nm) modes, though it should be noted that the characteristic modal diameter of each aerosol mode can evolve in response to aerosol and chemical processes.

The premise of the W22 scheme is to allow activation of Aitken mode particles in saturated updrafts so that they can act as CCN in the model. When — during activation — the number of Aitken particles at the critical diameter exceeds the number of accumulation mode particles, aerosols are shifted from the Aitken to the accumulation mode to enforce equality between the Aitken and accumulation mode concentrations at the critical diameter. Conceptually, this should place the Hoppel minimum at the critical diameter in strong updrafts. In weak updrafts, where the critical diameter is larger than the Hoppel minimum, no Aitken particles are moved into the accumulation mode.

For simplicity, we assume that all cloud droplets are associated with an accumulation mode aerosol, so the "Aitken" mode is composed of unactivated aerosols. Supersaturation, which helps to determine the critical diameter, is diagnostic and computed within the Morrison microphysics scheme (Wyant et al., 2022; Morrison et al., 2005). Typical supersaturation values experienced by CCN upon activation (i.e., mean supersaturation weighted by local activation rate) range across the BL from 0.07% to 0.2% for accumulation mode aerosols and 0.1% to 0.25% for Aitken mode aerosols transferred into the accumulation mode. Similarly, the typical updraft strengths during activation range from $\sim$0.1 to 0.6 m s^{-1} for accumulation and $\sim$0.2 to 0.8 m s^{-1} for Aitken mode aerosols.

A key distinction between this study and the more idealized W22 study is that our LES case is more tightly constrained by *in situ* observations in an effort to simulate aerosol-cloud-precipitation interactions in a context as similar to the real world as possible. Initial thermodynamic profiles of temperature and moisture are developed from a combination of the Graciosa Island soundings, ERA5 reanalysis soundings extracted to the campaign region (Figure S3), and *in situ* flight profiles. As initial simulations produced thinner-than-observed clouds, the moisture profiles were slightly enhanced to better correspond with the second, comparison portion of the observations (12-14:30 UTC) (Figure 1b, S1, S5b). The initial Aitken and accumulation mode aerosol number and mass mixing ratios (Figure S4a, b, S5c, d) follow the P2 reference profile from RF16 (star in Figure 1a). Modal Aitken and accumulation widths (as defined by geometrical standard deviation, σ_{ait}=1.3 and σ_{acc}=1.4 μm) and initial diameters (Table S1) are selected to correspond to case observations (Figure S4c). While the characteristic diameter of each aerosol mode may evolve, the modal widths are fixed in time. The initial SAM modes and the observed size distributions for P2 are shown in Figure S6, initial values are detailed in Table S1 and Figure S5c, d. N_d is initialized at 35 mg^{-1} based on the median *in situ* observations for the upper cloud layer (Figure S4d).

Simulations are initialized with a small, random moisture and temperature perturbation and run for 12 hours to allow the development of mesoscale variability. During this period, the domain-mean profiles of temperature, specific humidity, aerosol number and mass mixing ratios are nudged to the previously discussed, initial profiles (Figure S5) that capture key elements of the RF16 environment. Afterwards, nudging within the boundary layer and the inversion layer is switched off, so that the simulations are released to run freely at 9:00 UTC and throughout the remaining 12 hr duration of the simulation (ending at 21:00 UTC). Following Blossey et al. (2021), after release, each simulation is forced by the large-scale vertical velocity as well as moisture and temperature tendencies from ERA5 to maintain meteorology at real world conditions throughout the simulation, while nudging to the initial profiles only in the FT, starting 500 meters above the inversion. Although aerosols are affected by large-scale vertical motion, no large-scale horizontal advective tendencies are applied to the aerosol, so that, after a simulation is released, the aerosol evolves as a net balance between sources and sinks as in, e.g., Wood (2006).

For model-observation comparisons, SAM aerosol number concentrations are calculated as in Zender (2001) using aerosol size distributions truncated to specific instrument observation size ranges for Aitken (10-100 nm), accumulation (100-400 nm), and total (combined Aitken and accumulation ranges, 10-400 nm) aerosol. Where necessary, SAM profiles compared to observations are subset to in-cloud (LWC$\geq$0.01 g kg^{-1}) and out-of-cloud ($<$0.01 g kg^{-1}) samples (e.g., observed aerosol concentrations are only reported out-of-cloud while droplet number concentrations are only reported in-cloud). All size distributions from SAM are computed for the combined in- and out-of-cloud aerosol across the $x-y$ domain for each time and height level. For comparisons with observed size distributions, we have selected relatively cloud-free altitudes (i.e., the lower BL at 300 m, the transition layer between Cu and Sc cloud layers at 700 m, and the FT at 1.5 km). When comparing across sensitivity studies, altitudes dominated by cloud (i.e., 0.4

and 1.2 km) and aerosol budgets used to interrogate the simulations are also included in order to directly examine aerosol-cloud processing. Precipitation fluxes are calculated as the integral of sedimentation fluxes over cloud and rain droplet sizes, equivalent to observations.

The evolution of aerosol-cloud precipitation interactions are examined using number and mass budgets for Aitken and accumulation modes over several atmospheric layers. These budgets are formulated following W22. The accumulation mode in this context is composed of unactivated accumulation, in-cloud droplet, and in-rain aerosols. Thus, activation and droplet evaporation (which leaves behind unactivated accumulation mode aerosols) do not have a net impact on the budget. For each aerosol category, the number tendencies evolve following a rate equation:

$$\begin{aligned}\dot{N}_{Tot.} &= \dot{N}_{Ait.\ Trans.} + \dot{N}_{Top\ Flux} + \dot{N}_{Bot.\ Flux} + \dot{N}_{Wet\ Scav.} + \dot{N}_{Scav.} \\ &\quad + \dot{N}_{Coag.} + \dot{N}_{Large-Scale\ Sub.} + \dot{N}_{Sed.} + \dot{N}_{Nudge.} + \dot{N}_{Res.}\end{aligned} \tag{1}$$

This can be further simplified as:

$$\dot{N}_{Tot.} = \dot{N}_{Ait.\ Trans.} + \dot{N}_{Top\ Flux} + \dot{N}_{Bot.\ Flux} + \dot{N}_{Wet\ Scav.} + \dot{N}_{Other} + \dot{N}_{Res.} \tag{2}$$

The leading terms are activation or transfer of Aitken aerosol into the accumulation mode (*Aitken Transfer*), movement of aerosol through turbulent fluxes (*Top Flux* and *Bottom Flux* relative to the layer the budget is computed over), and removal of aerosol through autoconversion, accretion, and limiters (as in Berner et al., 2013) (*Wet Scavenging*). Tendency terms with small contributions are gathered for analysis purposes into the *Other* term. These are scavenging (in-cloud removal of interstitial and unactivated aerosol), coagulation (removal of aerosol through coalescence or aggregation of aerosols via Brownian motion), large-scale subsidence of aerosol from the free troposphere, sedimentation of aerosols out of the atmosphere, and nudging tendencies applied during the spin-up phase of the model (before 9:00 UTC). The residual captures the remaining behavior of the total aerosol tendencies and, when small, indicates that these equations capture the majority of the aerosol behavior. Note that the meaning of the turbulent fluxes change depending on the layer they are computed over (i.e, surface source, exchange between layers). The mass budgets have a similar formulation with an additional term for chemistry (particle growth through chemical processing):

$$\begin{aligned}\dot{M}_{Tot.} &= \dot{M}_{Chem.} + \dot{M}_{Ait.Trans.} + \dot{M}_{Top\ Flux} + \dot{M}_{Bot.\ Flux} + \dot{M}_{Wet\ Scav.} \\ &\quad + \dot{M}_{Scav.} + \dot{M}_{Coag.} + \dot{M}_{Lrg.-scale\ Sub.} + \dot{M}_{Sed.} + \dot{M}_{Nudge.} + \dot{M}_{Res.}\end{aligned} \tag{3}$$

Time evolution for all number and mass budget terms are shown in the supplement (Figure S7 and S8, respectively).

Aerosol sensitivity studies, described in Section 4, adjust the initial number concentration profiles. In each case, corresponding changes are made to the initial mass profiles so that the initial diameter and width of modes are identical across all simulations (Table S1). These changes to the initial aerosol profiles include halving the accumulation number while leaving the Aitken mode unchanged (*HfAc*), eliminating the Aitken mode while leaving the accumulation mode unchanged (*NoAit*), and halving the accumulation mode number while eliminating the Aitken mode (*HfAcNoAit*). To avoid computational issues, when Aitken aerosol is removed in the *NoAit* and *HfAcNoAit* simulations, Aitken number and mass are set to small, non-zero values. In the *HfAc* and *HfAcNoAit* simulations, both accumulation mass and number are halved relative to the vertically resolved *Ctrl* initial profile.

3 Simulating the RF16 ACE-ENA Case Study

We first present the general behavior of the standard SAM simulation for RF16 (hereafter *Ctrl*, Section 2.2). Figure 2 shows the evolution of aerosol and cloud droplet number along with the corresponding changes to horizontal variations in τ. Consistent with

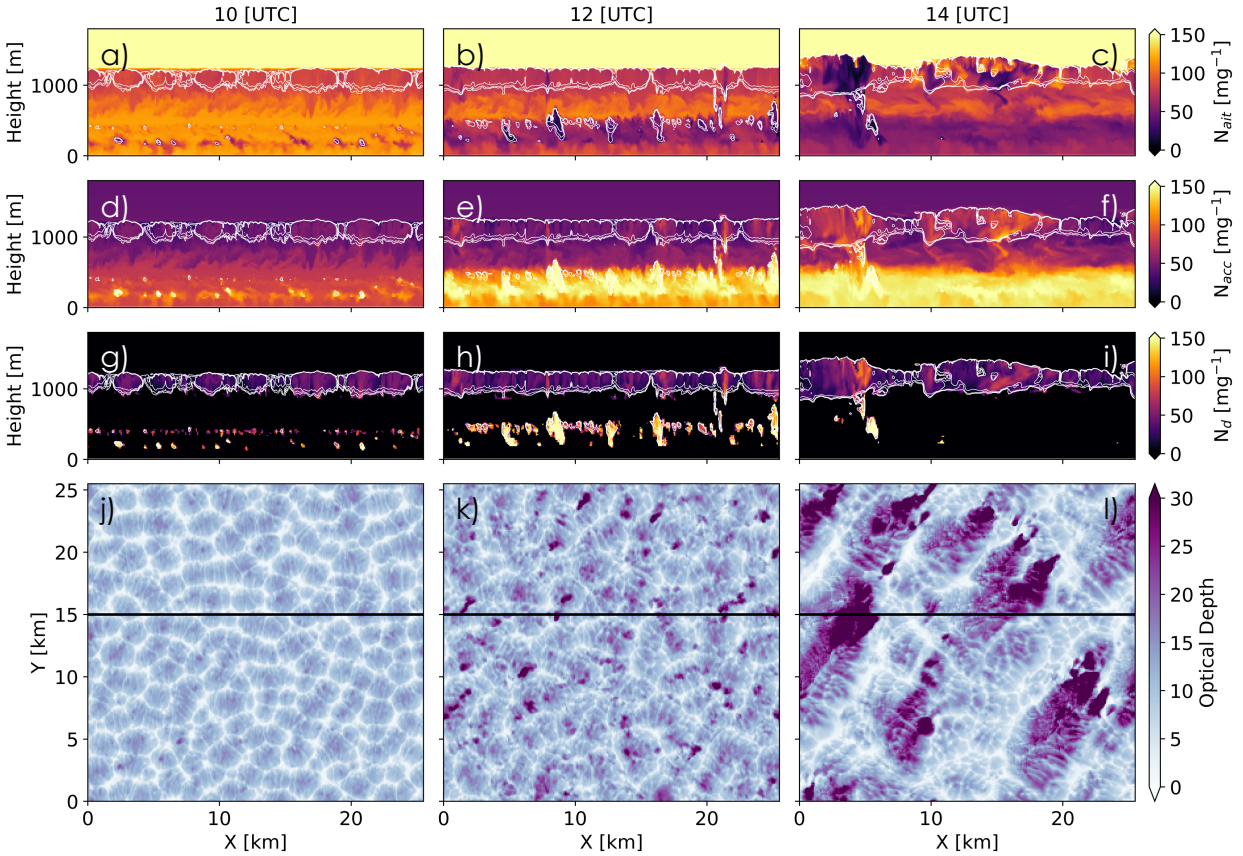

Figure 2. Vertical cross sections of SAM *Ctrl* simulation for Aitken (a-c), accumulation (d-f), and cloud droplet (g-i) number concentrations at 10:00 (a, d, g), 12:00 (b, e, h), and 14:00 UTC (c, f, i). Corresponding cloud optical depth spatial x-y snapshots for 10:00 (j), 12:00 (k), and 14:00 UTC (l). The black lines in (j-l) shows the location of vertical cross sections shown in (a-i).

observations, two cloud layers form: an upper, Sc layer between ∼ 1-1.25 km altitude and a shallow, Cu layer near the surface (∼250-500 m). Initially (∼ 10:00 UTC), N_{ait} is high in the FT and large throughout the BL (Figure 2a) while N_{acc} has the opposite structure (d). Over time, the Cu in the lower layer intensifies and drives local changes in aerosol size distributions (N_{ait} reduces while N_{acc} increases, b and e), increases in N_d (h), and formation of larger cumuli (e.g., 12:00, b, e, h, k) that subsequently rise into the upper Sc layer (e.g., 14:00 UTC, c, f, i, l). The upper layer deepens with time as Sc clouds grow larger and connect with Cu below. Eventually, more distinct Sc cells form (e.g., 14:00 UTC) with increased core N_d (i) and τ (l). Large-scale uplift (Figure S3a) likely encourages this cloud evolution. The *Ctrl* simulation appears to capture the stratified aerosol vertical distribution evident in the RF16 observations. N_{ait} is largest in the FT (Figure S1a, S4a) and contributes the most to the total aerosol magnitude (Figure 1b), significantly exceeding N_{acc} at most heights in the marine boundary layer (Figure S1b,S4a) as will be discussed further in Section 3.1. Our simulations will facilitate further examination of essential aerosol-cloud-precipitation processes at work in this decoupled low cloud regime (Section 3.2).

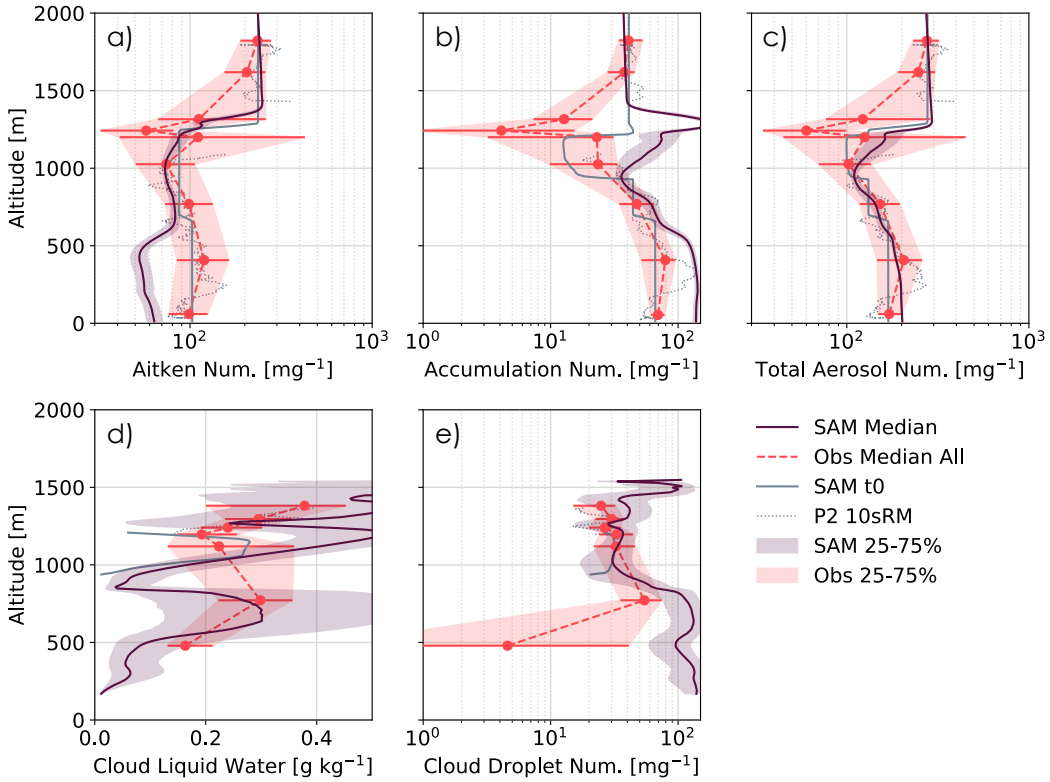

Figure 3. Model-observation comparison of median vertical profiles for select variables over 12-14:30 UTC: number concentrations of a) Aitken mode, b) accumulation mode, c) total aerosol (the sum of accumulation and Aitken aerosol modes), and e) cloud droplets; and d) cloud liquid water content. Aerosol comparisons are computed only for out-of-cloud samples while cloud liquid water content and droplets are only for in-cloud samples. Observations (red) are binned into ten quantiles by altitude and shown as a median (dashed line with dots) and an interquartile range (shading with horizontal lines) for each bin. SAM *Ctrl* (purple) is similarly shown as a median (line) with interquartile range (shading). Initial estimates are included for the observations (10-second running mean for profile 2, dashed grey) and SAM (initial profile from simulation, solid grey).

3.1 Observational Evaluation

Interrogating the *Ctrl* simulation with observations (Section 2.1, 2.2) informs us of the capabilities and limitations of our case study and model. Skill in reproducing the net behavior sampled during RF16 will give us confidence in our ability to capture the complex interplay of aerosol-cloud-precipitation processes driving the cloud system evolution in this regime.

Our first evaluation utilizes vertical profiles of several key quantities observed from the G-1 aircraft over the comparison period (12-14:30 UTC, Figure 3). The *Ctrl* median and interquartile range are compared with the observed median and interquartile range in ten altitude bins (which are used to account for differences in aircraft sampling frequency across the BL). Generally, median *Ctrl* profiles fall within the interquartile range of observed profiles at most levels. Agreement of out-of-cloud aerosol with observations

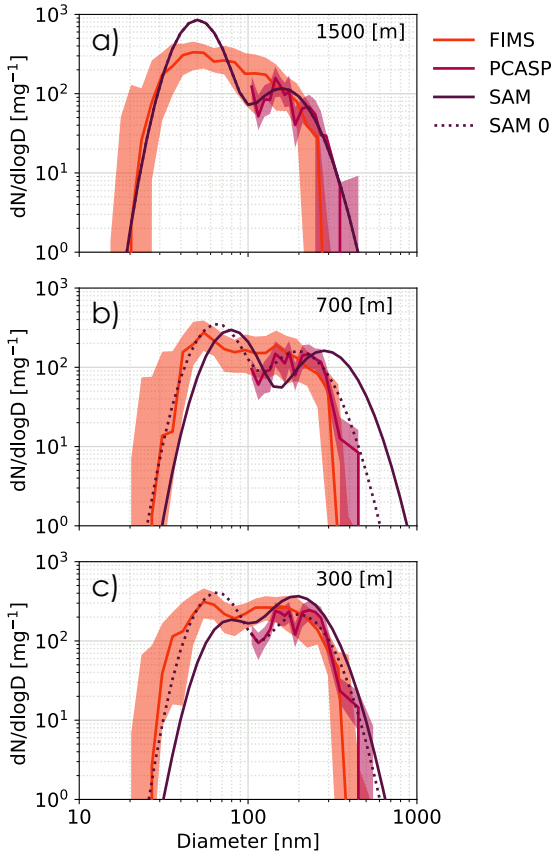

Figure 4. Model-observation comparison of median aerosol size distributions over 12-14:30 UTC at three levels: a) 1500 m, b) 700 m, and c) 300 m. Observations within 100 m of the labeled SAM altitude level are included. SAM *Ctrl* size distributions (purple) for the initial (dashed, Section 2.2)) and comparison period median (solid) are shown. Inclusion of the initial size distribution illustrates evolution of aerosols over the intervening time. Observations are included from two instruments on the G-1: the FIMS (orange) and the PCASP (pink) which, respectfully, resolve the majority of the Aitken and Accumulation mode sizes (Section 2.1). *In situ* values are shown as median (solid) and interquartile range (shading) over the comparison period.

appears to be especially strong (Figure 3a-c). Because the simulated aerosol state is critical in our study, it is worth examining this in more detail.

Total aerosol number concentrations (Figure 3c), the sum of Aitken and accumulation number (Figure 3a, b), coincides with observations across all altitudes and shows the best overall agreement of all variables examined. When aerosol number is separated into its individual modes, good agreement is found across most altitudes. Opposing deviations from observed behaviors are seen in the Aitken and accumulation size ranges in the BL between ∼0-500m: simulated Aitken aerosol number (Figure 3a) is depleted while accumulation number (Figure 3b) is augmented relative to observations. These deviations in *Ctrl* occur mainly in the lower, Cu cloud layer (e.g., Figure 2h). Smaller discrepancies are also found between observations and the *Ctrl* at the upper, Sc cloud level in accumulation number (∼1.25-1.5km, Figure 3b). As seen by the large observational

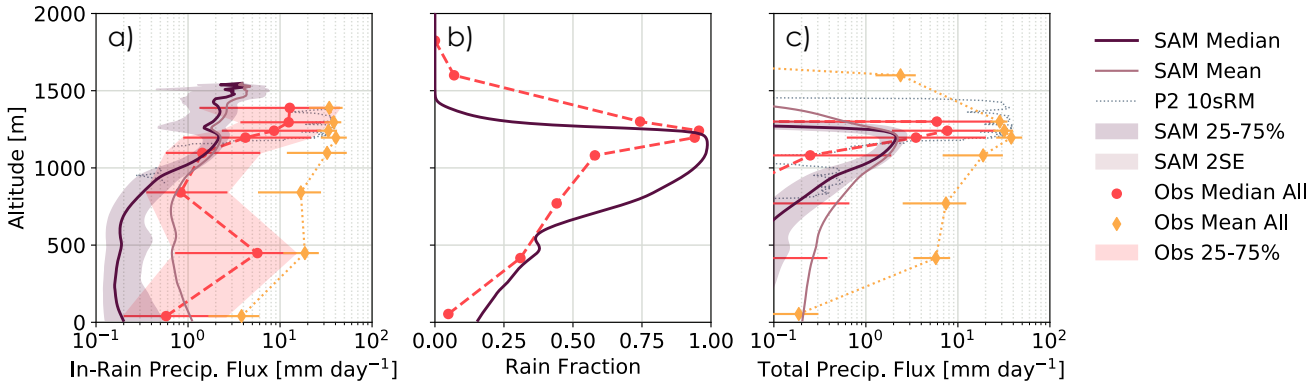

Figure 5. Model-observation vertical profile comparisons for precipitation measures over 12-14:30 UTC. Total profiles are computed (as in Figure 3) for: a) in-rain precipitation flux, b) rain fraction, and c) total precipitation flux. Rain is determined based on the conditional threshold, $P \geq 0.1$ mm day^{-1}. In addition to median and interquartile range, means are also shown (diamonds and dotted line for observations, thin line for SAM).

uncertainties in the upper cloud layer, however, observations at this altitude are impacted by limited opportunities for *in situ* aerosol sampling in cloud-free air.

Even though the Cu cloud layer occurs in both observations and SAM (e.g., Figure 1b, ∼500m quantiles in Figure 3d, e), this degree of modal aerosol partitioning is not seen in SAM. The depletion of Aitken aerosol (Figure 2a, b) and the accompanying increase in accumulation mode aerosol (Figure 2d, e) indicates sufficient updraft strength and supersaturation in the thin Cu layer occurs to enable Aitken activation through the W22 transfer scheme. This can also be seen in the evolution of the simulated aerosol size distribution at 300 m from its initial shape to the median behavior over the observation-comparison period (Figure 4c). The characteristic modal diameter for the Aitken mode moves toward the characteristic modal diameter for the accumulation mode, reducing overall Aitken aerosol number and the depth of the Hoppel minimum. While some activation likely occurs at this level, the magnitude of the deviation from observations suggests the simulated transfer is too efficient. This may, in part, reflect the complexity of initializing a rapidly evolving boundary layer (Section 5). The simulated aerosol partitioning agrees with observations elsewhere (Figure 3a, b), suggesting the parameterized Aitken transfer is operating reasonably at other altitudes.

Further examination of median aerosol size distributions over the observation comparison period show that the *Ctrl* partitioning is within the observed interquartile range at most sampled altitudes within the boundary layer. Note that the observed and simulated distributions overlap exactly in the FT due to nudging above the inversion (Figure 4a). The simulated size distributions in the transition layer at 700 m altitude (Figure 4b) and in the subcloud layer at 300 m altitude (Figure 4c) both shift away from their initial distributions. The relative changes in modal location indicate distinct underlying causes for these distribution shifts. At 300 m the Aitken mode decreases in number due to the parameterized transfer and shifts more strongly toward larger sizes than at 700 m. The accumulation mode shifts less toward larger sizes at 300 m. Processes driving the larger accumulation mode shift at 700 m will be examined in Section 3.2.

Ctrl cloud microphysical properties are also in good agreement with observations. In-cloud LWC (Figure 3d) is within 25-75% of observations across the BL, with a moister Sc layer and very similar Cu layer. N_d (Figure 3e) also agrees well with observations over

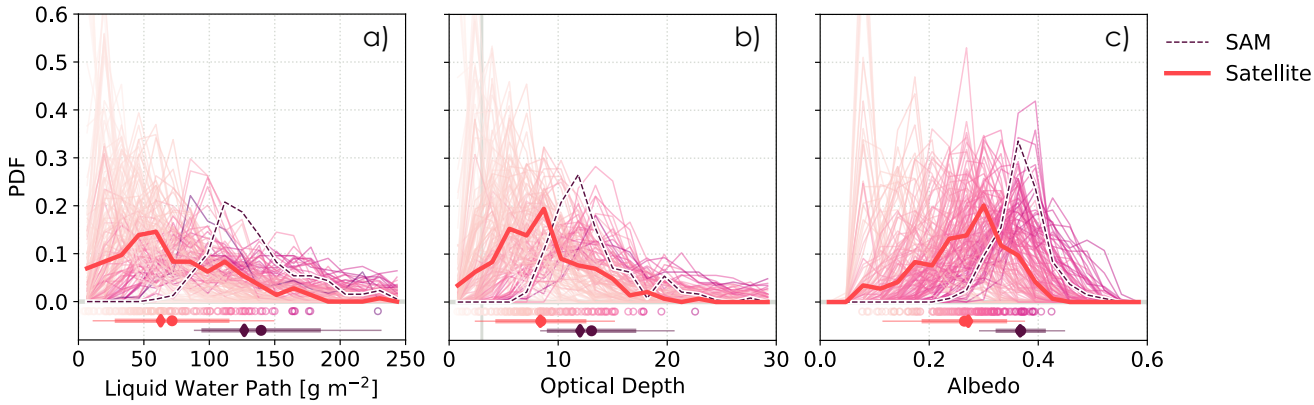

Figure 6. Model-observation comparison for satellite observations over 12-14:30 UTC: a) cloud liquid water path, b) cloud optical depth, and c) albedo. PDFs for each satellite subdomain (thin lines, colored by subdomain mean value) are shown along with their means (colored circles). A PDF constructed from the subdomain means (red) is shown along with descriptive statistics: mean (dot), median (diamond), standard deviation (thick line), and 5th-95th range (thin line). A PDF comparable to the subdomain PDFs is constructed from the *Ctrl* simulation coarsened to the satellite resolution (purple, thin dashed line). Model statistics for comparison to the observations are also included. See Section 2.1 for further sampling details. In b), the optically thin cloud threshold (τ=3) is shown as a grey line (O, Wood, & Tseng, 2018).

the BL, particularly in the Sc layer. There is a significant difference from the observations in the lowest observed quantile centered at ∼500 m altitude. This may be associated with sparse sampling of the Cu clouds occurring in this layer, as is evident from the large observational uncertainties. Because this is also where the *Ctrl* simulation exhibited over-prediction of accumulation aerosol, however, the generous N_d in this layer may be associated with that discrepancy. Overall, the good agreement in N_d across the majority of the BL suggests that the net balance between the evolving aerosol sources and sinks generated in *Ctrl* is realistic.

We can assess the simulated aerosol sinks in more detail using vertical precipitation profile comparisons (Figure 5, Section 2.2). More heavily precipitating rain events are defined where precipitation exceeds a conditional threshold ($P \geq 0.1$ mm day^{-1}), allowing us to examine in-rain precipitation flux (a), rain occurrence fraction (b), and total precipitation flux (c) separately. *Ctrl* tends to produce a smaller amount of rain (a) but is raining over a deeper portion of the BL than is observed (b). Note that cloud drop sedimentation is also included in the simulated and observed precipitation rate estimates. Total precipitation flux is within observed interquartile range throughout the BL (c). This suggests that *Ctrl* simulates a more consistently drizzling cloud system than the infrequent but heavily raining system observed during RF16. The separation between the mean and median estimates of both in-rain (a) and total precipitation flux (c) clarifies this difference in observed and simulated precipitation behaviors. The mean and median are significantly separated in observations: RF16 sampled a few heavily precipitating clouds (∼30 mm day^{-1}) but fewer lightly precipitating clouds (a, b), reducing the median total precipitation observed sub-cloud (c). *Ctrl*, in contrast, has closer mean and median behaviors: there are fewer heavily precipitating clouds produced compared to observations but more frequent drizzling clouds (b), increasing the median without skewing the mean toward higher values (a, c). In both *Ctrl* and observations, precipitation peaks at similar heights (b, c).

Finally, we can evaluate the *Ctrl* radiative properties over the comparison period using satellite observations. In order to capture the spread in cloud behavior across this case when using the coarser satellite data, we utilize 144 samples of comparable size to the simulation domain (0.25 x 0.25°) sampled within a 3 x 3° box overlapping the flight sampling region (Section 2.1). Subdomain means and PDFs indicate the spread in behavior seen in all three satellite retrievals for this region and time (Figure 6, S2). After coarsening the SAM output to the satellite resolution, we see that the *Ctrl* simulation (purple) tends towards the upper end of the observed behavior.

Because *Ctrl* N_d corresponds well with *in situ* observations (Figure 3e), we expected good agreement in the optical properties. However, the moisture of the clouds also matters to the overall radiative properties. *Ctrl* tends to simulate moister clouds (Figure 6a) with higher τ (b) and higher area-mean albedo (c). The tendency toward moister clouds is consistent with Figure 3d and the higher N_d values in the Sc layer (e), which was above the aircraft-sampled flight level. It is also worth considering that the satellite retrievals may miss the less frequent, more heavily precipitating (Figure 5) and moister Cu clouds observed by the aircraft. These are likely difficult for satellites to resolve as they are both small (<3 km) and potentially shielded by upper level Sc clouds.

Is the *Ctrl* simulation statistically likely to fall within observed subdomain variability? To test this, we use a PDF constructed from the subdomain means (red) and apply Welch's unequal variances t-test to compare the population means of the satellite samples and the simulation. In all cases, the *Ctrl* mean is the same as the satellite subdomain aggregate mean at 95% confidence. The *Ctrl* mean (circle) falls within the 5th-95th range from the satellite subdomain aggregate (thin line). Thus, the *Ctrl* simulation is consistent with satellite observed cloud property variability although it tends toward the moister and brighter observed cloud behaviors.

We conclude that the W22 configuration of SAM with this specified initialization method captures most of the key features of the decoupled low cloud regime sampled in RF16. *Ctrl* exhibits skill in generating and maintaining aerosol across the FT and the majority of the BL in both number and size distributions. The main exception is in the lower, Cu cloud layer where there is a discrepancy in aerosol partitioning between Aitken and accumulation modes due to Aitken particles being too readily activated. *Ctrl* also tends to produce a cloud with higher liquid water content and more drizzly than observed. Some of the forcings for this case study (i.e., imposed large scale uplift) and necessary initialization choices (i.e., BL moistening of reanalysis to resemble observations) likely encourage this macro-physical response. However, neither aerosol nor cloud differences from observations appear to negatively effect N_d or the net balance of aerosol sources and sinks. *Ctrl* produces cloud liquid water path, τ, and domain-mean albedo on the higher end of satellite observed ranges, but their statistical agreement with observed behaviors suggests SAM has sufficient skill to accurately analyze radiative property sensitivity to aerosol changes. The differences between observed and *Ctrl* behaviors will be revisited in Section 5. However, the fidelity of the *Ctrl* simulation in capturing aerosol and aerosol-cloud-precipitation interactions is sufficiently robust to justify further analysis: i) identifying key aerosol-cloud-precipitation processes in this morphology regime (Section 3.2) and ii) evaluating regime sensitivity to changes in aerosol conditions (Section 4).

3.2 Identifying Key Aerosol-Cloud-Precipitation Processes

Satisfied with the agreement between observations and our constrained aerosol-coupled LES for this case, we can examine the time evolution of aerosol-cloud-precipitation interactions and identify which processes dominate the behavior of this decoupled low cloud regime. Figure 7 shows the vertical, time evolving profile of N_{acc} (a) along with the Aitken transfer tendency term (b), updraft strength (i.e., vertical velocity variance, c), and N_{ait} (d). After release at 9:00 UTC, Aitken aerosol is transferred in many small Cu-layer up-

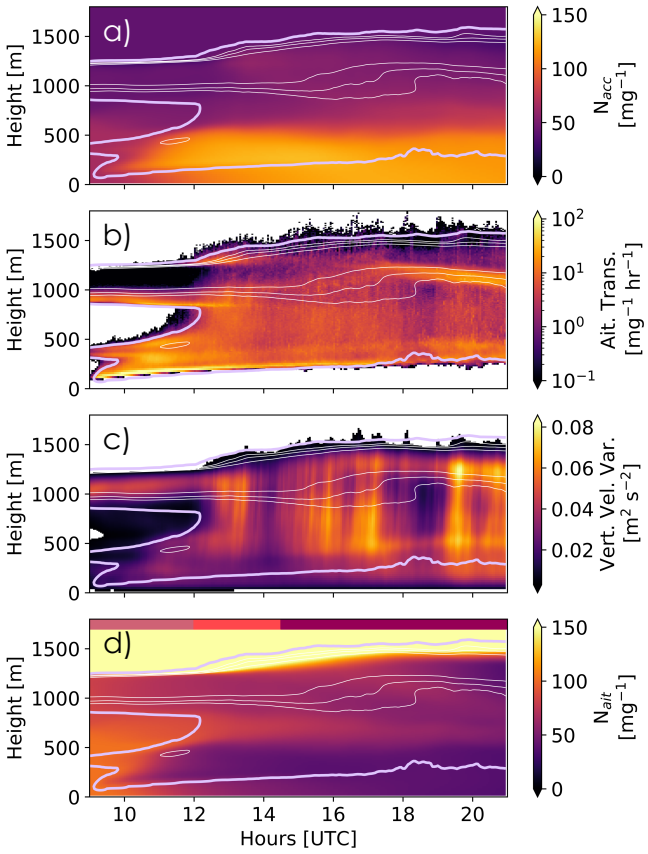

Figure 7. Time vs. altitude profiles showing the *Ctrl* evolution of a) accumulation number concentration (in and out of cloud), b) Aitken transfer rate, c) vertical velocity variance, and d) Aitken number concentration. Contours of 0.05, 0.1, and 0.2 g kg^{-1} liquid water (thin white lines) and 10% cloud cover (thick purple line) are included for reference. Three time periods are marked in d) for future reference: 9:00-12:00 (pink), 12:00-14:30 (red), and 14:30-21:00 UTC (dark red). Vertical velocity variance <0.003 m^2 s^{-2} and Aitken transfer <1 mg^{-1} day^{-1} are not shown.

drafts around ∼250 m altitude, rapidly depleting the initial Aitken BL aerosol. By 12:00 UTC, the Aitken transfer subsides to a more sustainable rate, and the aerosol layers begin to mix due to turbulent and convective fluxes. Towards the end of the simulation (after 16:30 UTC), Aitken activation and transfer increases in robust updrafts that develop in the Sc layer. However, N_{acc} does not increase simultaneously, suggesting that this N_{ait} activation is buffering aerosol and droplet number concentrations against precipitation depletion.

To delve further into aerosol processes affecting these two cloud layers and their interchanges, we calculate three atmospheric layer number budgets (Section 2.2, Figure S7) examining: i) the total depth, including the BL and lower FT (0 to 1.6 km, Figure 8a), ii) the upper layer (0.8 to 1.6 km, Figure 8b), and iii) the lower layer (0 to 0.8 km, Figure 8c) tendencies. A corresponding mass budget (Figure S8) is also computed and will be discussed where relevant. Figure 8 presents the mean tendencies of the leading terms (Eq. 2) contributing to the Aitken and accumulation number evolution. To aid in interpretation, we focus on the mean tendencies over three reference periods (highlighted in Figure 7d): after release (9:00-12:00), during the observation comparison (12:00-14:30),

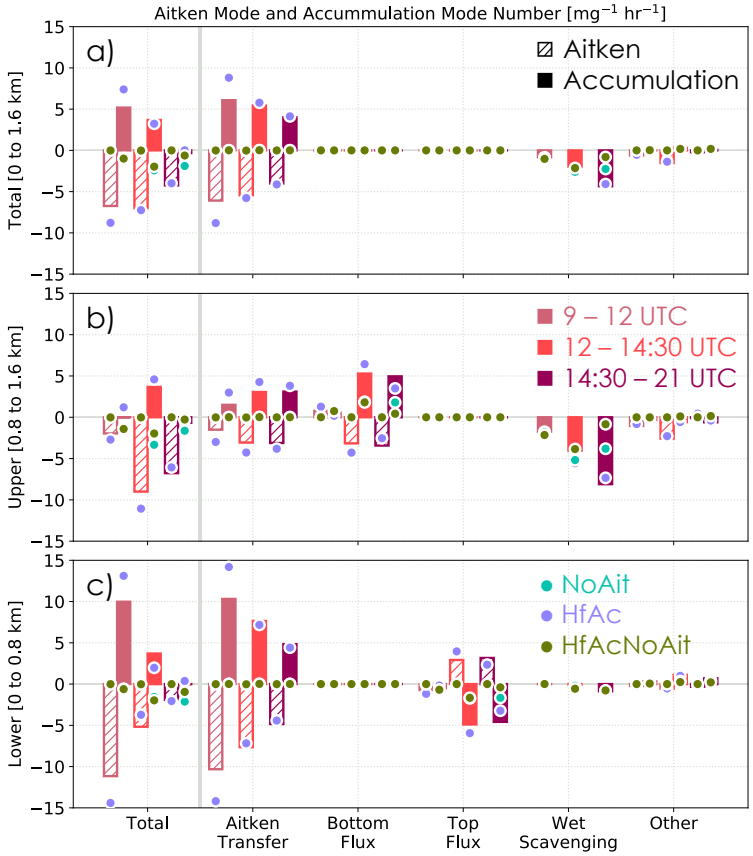

Figure 8. Evolution of leading number budget terms for Aitken (hatched) and accumulation (solid bars) modes computed over the total depth (a, 0 to 1.6 km), over the upper layer (b, 0.8 to 1.6 km), and over the lower layer (c, 0 to 0.8 km). Mean number tendencies are computed for the three time periods (left to right in each term category) highlighted in Figure 7d: 9:00-12:00 (pink), 12:00-14:30 (red), and 14:30-21:00 UTC (dark red). Bars show *Ctrl* mean tendencies while dots show equivalent values for the sensitivity studies (Section 4). Total tendency is to the left of the gray division line and contributions from individual terms are to the right. Companion plots for all number and mass tendency terms vs. time for all simulations are in the supplement (Figure S7 and S8).

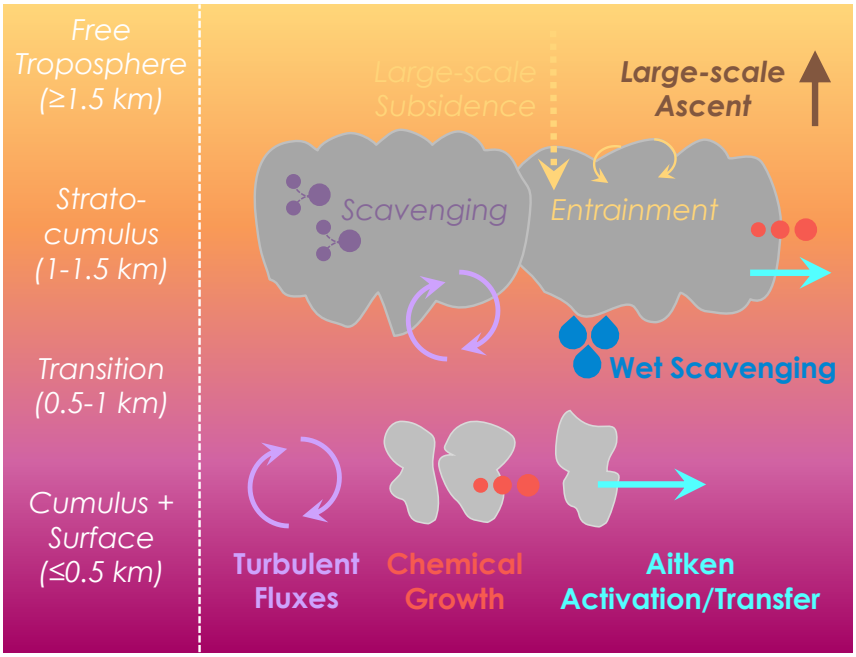

Figure 9. Key aerosol-cloud-precipitation processes involved in the evolution of the morphology regime observed during the ACE-ENA research flight on July 15, 2017 (RF16). The key terms shown are Aitken activation/transfer (occurring at all cloud layers), turbulent fluxes (eddies moving particles between layers), wet scavenging (aerosol depletion in rain), and mass growth through chemical processing. Scavenging (aerosol depletion in cloud), large-scale subsidence and entrainment of aerosols are included for completeness but only weakly contribute over this simulation's duration. Large-scale ascent of the environment, which encourages cloud moistening and increased organization, is also included.

and when accumulation sources and sinks are in quasi-balance (14:30-21:00 UTC). We also include a summary schematic illustrating these key processes (Figure 9).

Aitken transfer dominates the number tendencies in the total budget for both the Aitken (as a sink) and accumulation (as a source) modes. Aitken transfer decreases over time, with the fewest particles transferred to the accumulation mode during the final period. The removal of accumulation mode aerosol through wet scavenging simultaneously increases with time. The result is a gradual balancing between the Aitken transfer and wet scavenging accumulation number tendencies ($\dot{N}_{Tot.\ acc} \approx 0$) by the end of the simulation (14:30-21 UTC).

In all layers, the mass budget (Figure S8) is dominated by accumulation mode tendencies. Once activated, chemical processes quickly grow solute mass and diameter, committing the particles irreversibly to the accumulation mode and likely continuing to increase their size over time (e.g., Feingold & Kreidenweis, 2002) with potential assistance from collision-coalescence (e.g., Hoffmann & Feingold, 2023). Mass increases through chemical processing are partly offset by sedimentation removal. Similar to the number budget, mass is gained throughout the first two periods before the sources and sinks balance for the final period (except in the lower layer where $\dot{M}_{Tot.\ acc} > 0$).

Dividing the total budget into layers encapsulating the Cu (lower) and Sc (upper) clouds adds additional nuance to this story. Turbulent and convective fluxes act to mix and redistribute particles between layers. Aitken aerosols are exported from the upper

layer (bottom flux) into the lower layer (top flux). Accumulation aerosols are simultaneously fluxed in the opposite direction: exported from the lower layer into the upper layer. Aitken transfer dominates the lower layer but is of an equivalent magnitude to the turbulent flux and wet scavenging terms in the upper layer. Wet scavenging removes accumulation aerosol with increasing strength over time in both layers but is always much greater in the Sc layer. Because of different rates of change in the accumulation source (local Aitken transfer and turbulent fluxes) and sink (wet scavenging) tendency terms in the two layers, $\dot{N}_{Tot.\ acc} > 0$ in the lower layer until the final, quasi-balanced period ($\dot{N}_{Tot.\ acc} \approx 0$) while $\dot{N}_{Tot.\ acc} > 0$ only in the observation comparison period (12-14:30 UTC). This lag between layers is mainly due to the delay while Aitken aerosols are transferred in the lower layer and fluxed up. Local Aitken transfer rates also increase with time in the upper layer, assisting in resisting precipitation depletion effects. Note that in-cloud scavenging weakly reduces Aitken and, in the final period, large-scale subsidence of Aitken from the FT weakly increases Aitken number in the upper layer (Figure S7c). A longer entrainment period or a larger FT Aitken concentration would be necessary to balance transfer loss and restore BL Aitken aerosol (see W22 sensitivity studies, Section 5). In this case, Aitken is lost at all levels and times ($\dot{N}_{Tot.\ ait} < 0$).

To summarize (Figure 9), in this decoupled low cloud regime Aitken mode aerosol is activated into the accumulation mode and grown through chemical processing in both Cu and Sc cloud layers. Turbulent and convective eddies mix Aitken aerosols down from the upper layer into the lower layer where they are transferred to the accumulation mode. Simultaneously, eddies export accumulation particles up into the transition and Sc layers where they are activated into droplets in updrafts. Precipitation depletion through wet scavenging removes accumulation aerosol in Sc (and weakly in Cu), balancing the increase in BL accumulation particles from Aitken transfer. This resistance to precipitation loss and the accompanying maintenance of N_d associated with Aitken activation into the precipitation-depleted accumulation mode is a hallmark of the Aitken-buffering mechanism (McCoy et al., 2021).

4 Sensitivity Studies

In this section, we build on the *Ctrl* simulation with three additional simulations that examine the sensitivity of the RF16 cloud system and its aerosol-cloud-precipitation processes to changes in accumulation and Aitken aerosol number concentrations (Section 2.2, Table S1). *HfAc* reduces the initial *Ctrl* accumulation number by half throughout the entire profile. It asks whether the amount of Aitken aerosol in *Ctrl* can still buffer the aerosol-cloud-precipitation system against precipitation depletion in a reduced accumulation-mode environment. *NoAit* removes Aitken aerosol throughout the entire initial profile and tests whether Aitken aerosol is important to sustaining the accumulation profile against precipitation depletion. *HfAcNoAit* uses the accumulation profile of *HfAc* and the Aitken profile of *NoAit* to evaluate whether the aerosol and cloud profiles can be sustained against precipitation removal in the reduced accumulation case *without* the help of Aitken aerosol.

Differences between these simulations are immediately apparent from the time series of certain key parameters (Figure 10). Two types of behavior are encapsulated by these simulations: Aitken-buffered (*Ctrl*, *HfAc*) and Aitken-deficient (*NoAit*, *HfAcNoAit*) systems. When Aitken aerosols are present, the Aitken-buffering mechanism helps clouds to maintain coverage (a) despite depletion of cloud liquid water (c) through persistent precipitation (b). Aitken aerosol is steadily lost over time in *Ctrl*, *HfAc* and most of it is transferred to the accumulation mode, whose concentration remains nearly constant throughout these two simulations (e). Aitken transfer even enhances the initial accumulation number concentrations over time ($\sim$50 to $\sim$70 mg^{-1} in *Ctrl*, $\sim$25 to 55 mg^{-1} in *HfAc*). In contrast, the Aitken-deficient simulations (*NoAit*, *HfAcNoAit*) have significantly different cloud fraction evolution, beginning to break up at $\sim$14:30 and 12:00 UTC respectively (a). They steadily lose accumulation aerosols due to precipitation depletion

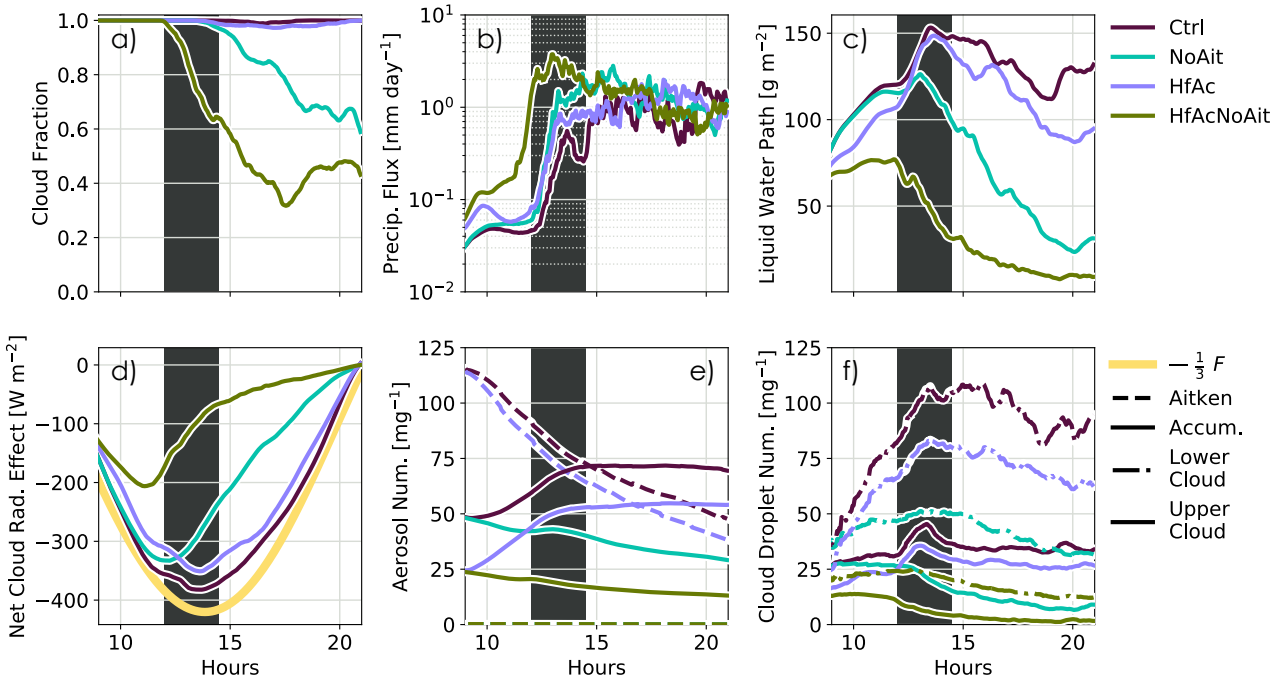

Figure 10. Time evolution of key SAM parameters for *Ctrl*, *HfAc*, *NoAit*, and *HfAcNoAit* simulations: a) cloud fraction, b) precipitation flux at the surface, c) liquid water path, d) net cloud radiative effect, e) Aitken (dashed) and accumulation (solid) aerosol number concentrations, and f) mean droplet number concentration in the upper Sc ($\geq$0.8 km, solid) and lower Cu ($\leq$0.8 km, dash dot) cloud layers. Observation comparison period shown in dark gray (12-14:30 UTC). Top of atmosphere incoming solar radiation (F, W m^{-2}) scaled by $-\frac{1}{3}$ is included on (d) for diurnal cycle reference.

being uncompensated by Aitken transfer. The trend in accumulation mode for all simulations is reflected by N_d in the upper Sc and lower Cu cloud layers (Figure 10f).

Snapshots at 14:00 UTC (Figure 11) highlight the differences in aerosol and cloud morphology across the simulations. Compared to *Ctrl*, all studies exhibit more distinct upper level mesoscale cells with a larger proportion of optically thin cloud layers. *HfAc* maintains cells similar to those in *Ctrl*, albeit with more cell separation and slightly lower τ. Clouds in the Aitken-deficient cases are much more heterogenous than in the Aitken-buffered ones. *NoAit* has much smaller cells and a reduced cloud cover with lower τ while the Sc in *HfAcNoAit* has already collapsed by 14:00 UTC, leaving the BL dominated by small cumuliform with a few optically thin layers left over from precipitation-depleted clouds.

Notably, the Aitken-buffered *HfAc* case loses less N_d, LWP, cloud amount, and NetCRE compared to the Aitken-deficient *NoAit*. The reason for this is apparent from Figure 10e: strong initial Aitken transfer has already restored the halved accumulation number by 12 UTC when precipitation begins to develop. Ultimately, the total aerosol number is what matters for the system, which is why the Aitken-buffering mechanism is effective. Access to Aitken aerosol in *HfAc* is a larger deterrent against precipitation depletion of N_{acc} and N_d, even at reduced initial accumulation numbers, than access to the full accumulation concentration in *NoAit*. *HfAcNoAit* takes this to the extreme, halving both accumulation number and removing the sustaining Aitken influence. Without Aitken aerosol

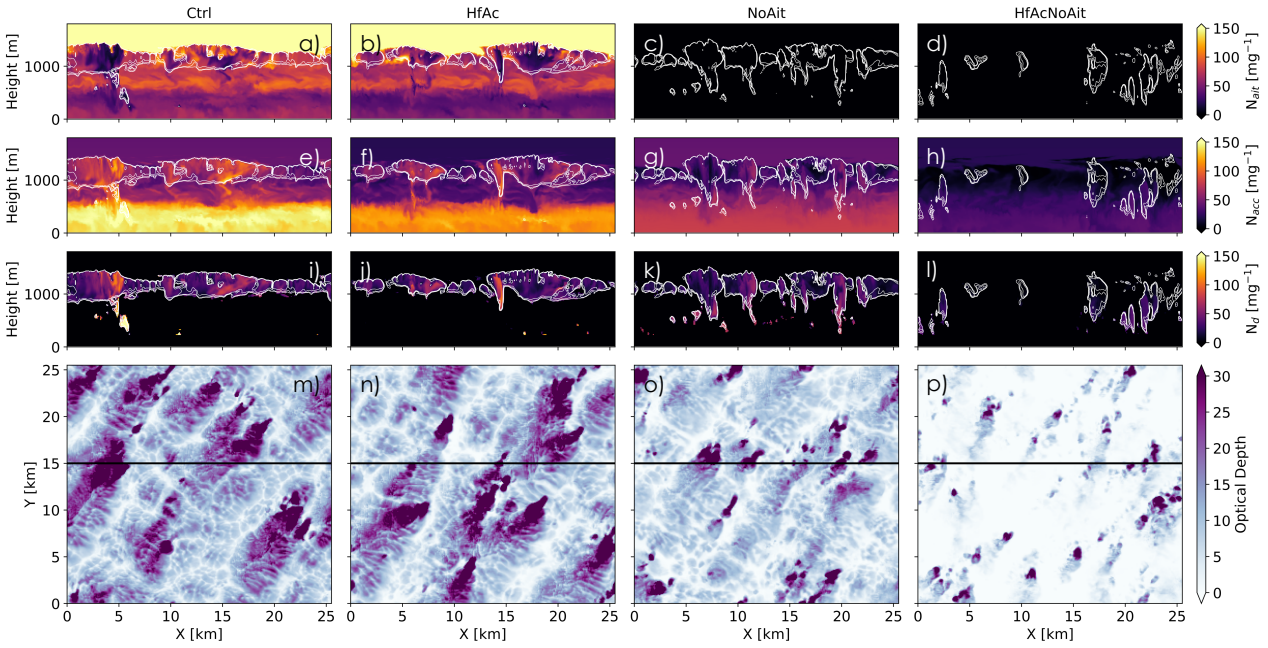

Figure 11. Cross sections of SAM sensitivity studies at 14:00 UTC as in Figure 2: *Ctrl* (a, e, i, m), *HfAc* (b, f, j, n), *NoAit* (c, g, k, o), and *HfAcNoAit* (d, h, l, p). Parameters shown are Aitken (a-d), accumulation (e-h), and cloud droplet (i-l) number and cloud optical depth (m-p).

to restore accumulation aerosol, the *HfAcNoAit* cloud system cannot resist precipitation depletion and has the largest loss signatures of all the simulations.

For all cases, N_d is higher in the Cu than the Sc. This is not unexpected based on the net gain in Cu accumulation seen in the *Ctrl* budgets (Figures 8, 9). We can examine the sensitivity study tendencies in more detail by contrasting their budget results (dots in Figure 8) and size distribution evolution (Figure 12).

In general, *HfAc* budgets behave the same as the *Ctrl*. However, it has a much larger initial Aitken transfer (9-12 in Figure 8a and c, 9-12 and 12-14:30 in b), which is consistent with the system compensating for the smaller initial accumulation number, as discussed previously. By the final period, the tendencies have returned to the *Ctrl* levels and the continuing Aitken transfer and turbulent fluxes are balancing the loss of accumulation through wet scavenging. The size distribution evolution in the Sc layer is the same between *Ctrl* and *HfAc* over 9-14 UTC (Figure 12b). In the Cu layer, in contrast to the *Ctrl*, *HfAc* transfers more Aitken aerosols to the accumulation mode such that the two distinct, initial aerosol modes are no longer maintained and the Hoppel minimum is lost by 14 UTC (Figure 12c). *HfAc* turbulent fluxes are also larger over this period (12-14:30 UTC in Figure 8b, c), helping to redistribute particles between layers and maintain the accumulation mode in the same location as the *Ctrl* (Figure 12b, c). *HfAc* budget and distribution tendencies are confirmation of both where the largest transfer occurs in the system (in the Cu layer before turbulent fluxes redistribute particles) and how the transfer adjusts in order to restore depleted accumulation aerosol and buffer the cloud system.

Under Aitken-deficient conditions (*NoAit*, *HfAcNoAit*), precipitation depletion leads to a loss of accumulation number at all levels (Figure 8). Turbulent fluxes still move accumulation number from the Cu to the Sc layer but the import of accumulation number is insufficient to offset removal through wet scavenging in the Sc. Precipitation-driven

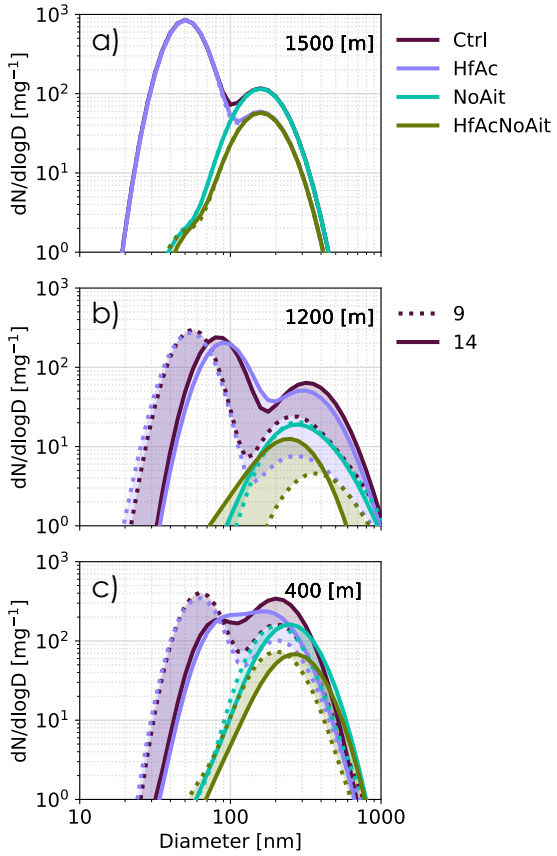

Figure 12. SAM size distributions evolving (shading) from 9:00 (dotted) to 14:00 UTC (solid line) for sensitivity studies: *Ctrl*, *HfAc*, *NoAit*, and *HfAcNoAit*. Distributions are shown at three levels: a) the FT at the top of the total and upper layer budgets (1.5 km), b) near Sc in the middle of the upper layer budget (1.2 km), and c) near Cu in the middle of the lower layer budget (0.4 km).

cloud breakup is hastened in the Cu layer (Cu N_d declines more precipitously than Sc N_d, Figure 10f) as a result of accumulation export through turbulent fluxes in the absence of restorative Aitken aerosols. Over 9-14 UTC, the Sc accumulation mode shrinks and shifts left under the influence of precipitation depletion (Figure 12b). Wet scavenging depletes the lower total aerosol number case more rapidly over this time period (Figure 10b, e) resulting in a larger modal shift for *HfAcNoAit* than *NoAit* (Figure 12b). The smaller *NoAit* modal shift in the Sc and the shift to the right in the Cu layer for both *NoAit* and *HfAcNoAit* may also be due to aerosols gaining mass through chemical processing, still a significant influence over this period before too many aerosols are lost (Figure S8). The *NoAit* and *HfAcNoAit* tendencies confirm that without Aitken aerosols, the cloud system undergoes more rapid collapse and the redistribution of particles through turbulent fluxes helps to accelerate collapse rather than resupply new accumulation aerosols as in the Aitken-buffered system.

The impact of Aitken buffering on radiation is seen in the diurnally varying net cloud radiative effect (NetCRE) (Figure 10d). *HfAc* produces a similar radiative response to *Ctrl*. In contrast, NetCREs for *NoAit* and *HfAcNoAit* are considerably smaller in magnitude with shapes dictated by their cloud break-up (a). *NoAit* and *HfAcNoAit* NetCREs

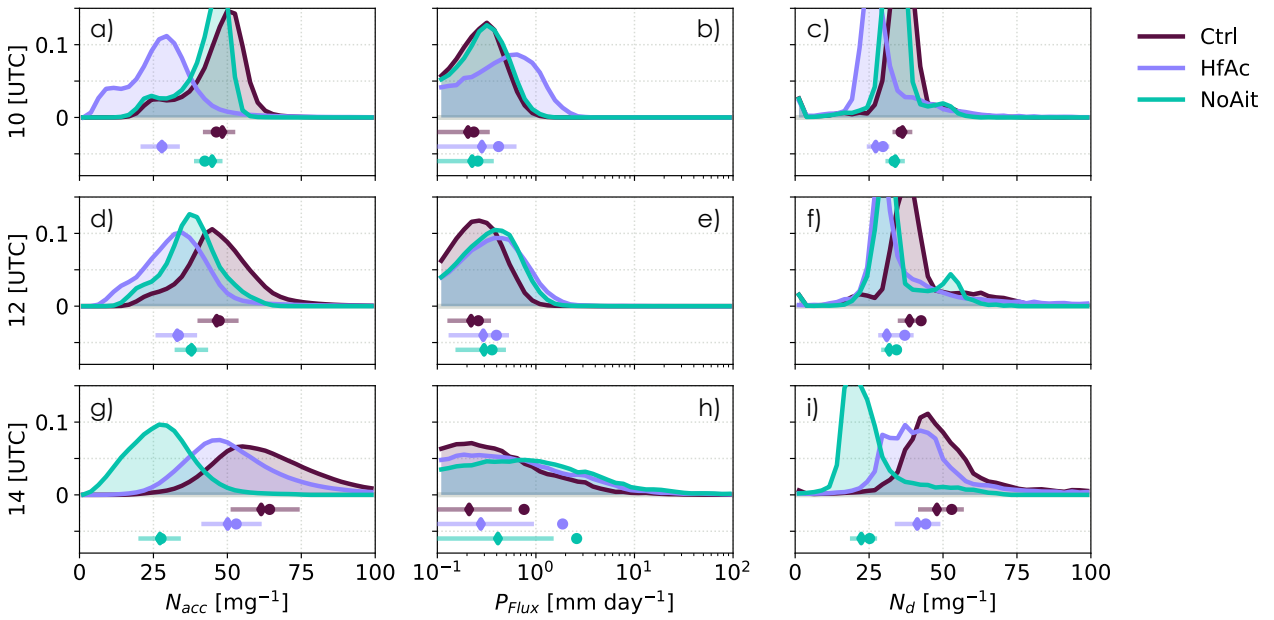

Figure 13. PDFs at native model resolution for the *Ctrl*, *HfAc*, and *NoAit* simulations at 10:00 (a-c), 12:00 (d-f), and 14:00 UTC (d-i). N_{acc} (a, d, g) and N_d (b, e, h) are for all values in the upper cloud layer (≥0.8km) while precipitation flux (c, f, i) is through the bottom edge (0.8 km).

peak just before precipitation flux substantially increases (b) and dissipates the cloud layer (a, c, e).

We can examine this radiative evolution, and its contributing factors, in more detail using the time evolution of the PDF of key variables over the observation comparison period (Figures 13, 14). Because the *HfAcNoAit* simulation is already collapsing at 12:00 UTC, we focus on contrasting the still evolving simulation behaviors of the *Ctrl* with *NoAit* and *HfAc*. Figure 13 highlights the aerosol-cloud-precipitation evolution we expect from these three sensitivity studies (e.g., Figures 8, 10). As precipitation increases over time (b, e, h), *HfAc* N_{acc} (a, d, g) and N_d (c, f, i) PDFs shift toward *Ctrl* PDFs. By 14:00 UTC, the mean and median *HfAc* are within the 25-75% range of *Ctrl*. In contrast, *NoAit* N_{acc}, N_d PDFs shift to the left, away from the *Ctrl*, in response to increasing precipitation depletion. Aitken aerosol presence is critical for sustaining N_d in the *Ctrl*, *HfAc* simulations, as evidenced by the swap in PDF location between *NoAit* and *HfAc* by 14:00 UTC.

Aerosol behavior controls the ability to sustain cloud homogeneity (Figure 11, 14h) and NetCRE (Figure 14i). However, an additional trend in LWP evolution (Figure 14a, d, g) adds nuance to this interpretation. LWP tends to increase in *Ctrl* and *HfAc* (Figure 10b, Figure 14a, d, g), a marker of cloud moistening due to meteorological uplift increasing mesoscale circulation and moisture convergence in this regime. Sc cloud development and moistening is also reflected in the broadening distribution and increasing mean and median magnitudes of τ (Figure 14b, e, h), NetCRE (Figure 14c, f, i), and precipitation flux (Figure 13b, e, h) with time. However, *NoAit* does not experience this moistening trend for as long as the other simulations. Instead, increasing precipitation (larger from 12-14 UTC for *NoAit*) has sufficiently depleted cloud water (Figure 13g) and N_d (i) by 14:00 UTC that τ (Figure 14h) and NetCRE (i) magnitudes are substantially reduced. More optically thin cloud layers (larger percentage with $\tau \leq 3$, h) are also

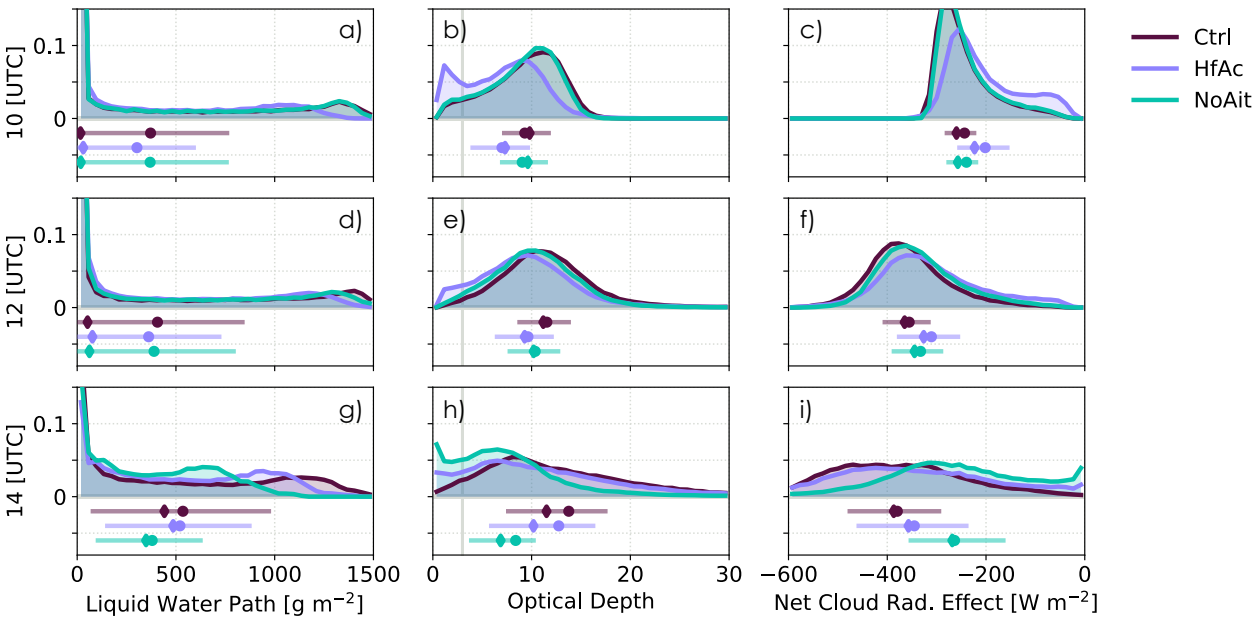

Figure 14. As in Figure 13 but for the: liquid water path in the upper Sc layer (a, e, i, for ≥0.8 km), cloud optical depth (b, f, j), and net cloud radiative effect (c, g, k). A grey line in b, f, j) references the optical depth threshold (τ=3) for optically thin clouds (O, Wood, & Tseng, 2018).

generated in *NoAit* by 14:00 UTC, consistent with more heterogeneous clouds (Figure 11c, g, k, o). Thus, we conclude that the increase in brightness and ultimate radiative effect of clouds in the *Ctrl* and *HfAc* simulations is driven by two essential mechanisms: i) cloud moistening due to meteorological uplift, and ii) cloud homogeneity maintained by Aitken aerosols buffering N_{acc} and N_d against precipitation depletion.

5 Discussion

5.1 Buffering Timescales

In this decoupled Cu rising into Sc case, processes influencing cloud and aerosol evolution operate over hours. Rapid aerosol evolution is driven by Aitken activation, turbulence, precipitation depletion, and chemical processing (Figure 9). Precipitation loss begins to impact accumulation number and mass after 14:30 UTC in the *Ctrl* simulation. The system is still buffered against cloud break-up, however, as depletion is approximately balanced by Aitken transfer and turbulent fluxes in this final period (Figure 8).

Intriguingly, the FT aerosol state appears to have limited impact over the duration of this simulation, with large-scale subsidence contributing Aitken only at the end (>14:30 UTC, Figure S7a, c). Peaks in Aitken concentration near cloud top (e.g., at 14:00 UTC, Figure 2c) and in Aitken transfer profiles (Figure 7a) suggest that entrained Aitken aerosol can directly buffer precipitation-depleted clouds (i.e., CCN-depleted supersaturated updrafts may be sufficient to activate locally entrained Aitken particles at cloud top).

The W22 10-day simulations found that large sources of Aitken particles, either from FT import (FT Aitken set to 1000 mg^{-1}) or surface production (10× surface source) could prevent BL cloud collapse in a subtropical, meteorologically quiescent regime. Our

Ctrl simulation, particularly the exponential Aitken number depletion signature (Figure 10d), resembles the W22 *BL1000* sensitivity study where BL Aitken concentrations were set to 1000 mg^{-1} while FT and surface sources were kept small. Cloud breakup was delayed in *BL1000* for twice as long as the control (8 vs. 4 days), suggesting that cloud breakup will be delayed in our case too even without large FT or surface Aitken sources. Our initial BL Aitken aerosol ($\sim$100 mg^{-1}, averaged over surface and transition values from the initial Aitken profile, Table S1) was either brought in from the FT over the past few days, generated from sea spray production (Lawler et al., 2021; Xu et al., 2022), or formed via new particle formation in the ultra-clean outflow at cloud edges (Kazil et al., 2011) or within the BL (Zheng et al., 2021). Since our model neglects the new particle production mechanism and has a very small surface source of Aitken aerosols in this weak-wind case, it is best used to quantify FT influence.

Our *Ctrl* budgets (Figure 8) show that $\sim$54 mg^{-1} of Aitken mode aerosol particles were transferred to the accumulation mode over the period from 9-21 UTC. This represents more than half the initial Aitken value within the boundary layer (Table S1), with approximately one third $\sim$30 mg^{-1} transferred from 9:00 to 14:30 UTC. By calculating the entrainment flux of aerosols during the simulation, we can find whether FT entrainment can balance these losses and, if not, estimate how many days worth of FT Aitken entrainment are consumed during this event. Because our budgets are formulated over an atmospheric layer that includes the BL and lower FT, we separately compute the entrainment source of aerosol using estimates of the entrainment rate and the jump of aerosols across the inversion. [1] Entrainment from the FT increases Aitken aerosol in the BL by $\sim$32 mg^{-1} over 9-21 UTC with most of that entrainment ($\sim$20 mg^{-1}) occurring between 9-14:30 UTC. Aitken transfer consumes almost twice as many Aitken aerosols as are entrained over the full 12 hour simulation. If the existing Aitken aerosol within the BL is derived from FT entrainment on preceding days, this Aitken transfer is equivalent to $\sim$0.9 days of FT Aitken entrainment (assuming the average magnitude during the simulations). Note that similar accumulation mode estimates show FT entrainment very weakly dilutes BL accumulation concentrations ($\sim$1.7 mg^{-1} lost over 9-21 UTC, ~ -3.4 mg^{-1} day^{-1}) which is consistent, albeit much smaller in magnitude, with FT accumulation dilution found in similar cloud structures in marine cold air outbreak outflows (Tornow et al., 2022).

One can imagine that an air mass might experience increasing Aitken aerosol concentrations during non-precipitating periods which might be consumed during periods of stronger forcing and precipitation. In this way, Aitken buffering of marine BL clouds may be accomplished, in part, with pre-existing Aitken mode aerosols that were entrained from the FT in the preceding days, as is the case here. However, we would note that, at this latitude, the FT Aitken number is observed to have concentrations of $\sim$210 cm^{-3} with accumulation number concentrations of $\sim$250 cm^{-3} (Heintzenberg et al., 2000) suggesting there is an additional source of Aitken aerosols that assists in balancing this BL sink (e.g., new particle formation, Zheng et al., 2021).

Expanding on this idea, we note that the above estimation assumes FT Aitken import only occurs locally, neglecting the substantial particle import that occurs with the passage of mid-latitude cyclones (e.g., Covert et al., 1996). Zheng et al. (2021) estimate that in post-frontal open cellular clouds occurring in the ACE-ENA region, where you

[1] The aerosol source due to FT entrainment is $N_{a,entr} = \rho(z_{ct})\, w_e\, \Delta(N_a)/M_{BL}$ where z_{ct} is the stratocumulus cloud top height, ρ the density, w_e the entrainment rate, $\Delta(N_a)$ the jump in aerosol number mixing ratio across the cloud top using 100m above and below z_{ct} as reference, and M_{BL} the BL mass per unit area. Because the observationally-derived initial θ sounding includes multiple inversions (Fig. S5a) and an inversion height based on the maximum θ_l gradient evolves irregularly, z_{ct} is used as a proxy for the inversion height and is defined as the height where the fraction of columns with 0.2 g m^{-2} of liquid above that height exceeds 25% of the shaded cloud fraction (based on the same LWP metric). Entrainment is computed as $w_e = d(z_{ct})/dt - w_{ls}(z_{ct})$ where w_{ls} is the large-scale vertical velocity.

are most likely to experience FT import after the passage of a cyclone, it takes 30-45 hours for FT air to replace the air in a 2 km deep BL. Assuming that the FT concentration of our initial profile ($\sim$250 mg^{-1}, similar to Heintzenberg et al. (2000)) is somewhat representative over this region for this season, we estimate a post frontal entrainment rate of 130 to 200 mg^{-1} day^{-1} which is, respectively, a factor of 1.2 to 1.8 greater than the Aitken transfer rate during our case (~ -112 mg^{-1} day^{-1}). Aitken transfer during our case would consume $\sim$0.3 to 0.4 days of Aitken aerosol entrained under post frontal conditions. This, even excluding new particle formation at cloud edges (e.g., Kazil et al., 2011) or in the BL (e.g., Zheng et al., 2020), emphasizes that Aitken aerosol can be frequently replenished and that Aitken buffering is likely to be both feasible and important in this region.

5.2 Challenges of Simulating Real-World Case Studies

We encountered a few challenges in simulating this case, in part due to a unique combination of factors. First, the detailed aerosol-cloud-precipitation observations for this morphology regime were taken over a relatively short time period. Second, this regime was rapidly evolving, in part due to the non-trivial meteorological forcing experienced throughout. This made using observations to both initialize and interrogate our simulation complicated, which leads us to an important question about our model construction and its limitations: is our initialization appropriate?

As noted previously, substantial and immediate Aitken transfer occurs in our simulation (e.g., Figure 7, 8), contributing significantly to the mis-partitioning of Aitken aerosol into the accumulation mode in the lower BL compared to observations (Figure 3a, b). An alternative initialization method that releases on a slow manifold instead of the current, fast transient may result in a less extreme initial transfer. Another method would be to select size distribution parameters in order to reduce the initial overlap between the Aitken and accumulation modes, reducing the initial transfer rate, while still capturing the majority of the observed PDF. Neggers et al. (2019) selects initial values using a technique that could be successful in our case. They initialize many, short-duration, Lagrangian simulations with varying initial states upwind of an observation platform and select conditions producing the smallest biases.

We expect that a more carefully tuned initialization method would have a minor impact on our results, however, and the main improvement would be in reducing model-observation aerosol biases in the lower BL. Model-observation consistency elsewhere in the BL and for other parameters (especially N_d, the net balance between aerosol sources and sinks) suggests that the model is credible and has skill. Thus, we expect the key mechanisms driving aerosol-cloud-precipitation evolution in this regime and their sensitivity to large changes in the initial aerosol profile (i.e., no Aitken, halved accumulation) are robust.

6 Summary

We utilize the System for Atmospheric Modeling (SAM) large eddy scale (LES) model with a novel Aitken-mode enabled microphysics scheme (Wyant et al., 2022, hereafter W22) to investigate a summertime mid-latitude decoupled low cloud regime observed during the ACE-ENA flight campaign (Wang et al., 2022). On July 15, 2017, the G-1 aircraft sampled an evolving cloud system composed of cumulus (Cu) rising into stratocumulus (Sc) under heightened Aitken aerosol concentrations (100-200 mg^{-1}) (Figure 1). *In situ* aircraft observations and satellite retrievals were used to develop and evaluate our case study.

We examined whether a large concentration of boundary layer (BL) Aitken aerosols impacted the evolution, radiative properties, and heterogeneity of this cloud system. Us-

ing observations to constrain our case study as well as realistic meteorological forcing, we found that the W22 aerosol-coupled SAM captured key time-evolving processes driving BL cloud and aerosol evolution. Profiles of total aerosol number matched observed evolution throughout the BL depth. Aerosols tended to be over-partitioned into the accumulation mode in the Cu layer due to excessive simulated transfer of Aitken particles to the accumulation mode in supersaturated updrafts, but were within observational uncertainties elsewhere. Simulated cloud liquid water was also within the upper end of the observed range, leading to clouds that were brighter and optically thicker but still within the observed interquartile range. SAM simulated more light precipitation than observed, likely due to aircraft sampling being dominated by a few heavily precipitating clouds. SAM cloud droplet number concentrations matched observations, indicating aerosol and microphysical discrepancies did not ultimately skew the net balance of cloud condensation nuclei (CCN) sources and sinks.

We identified the key aerosol-cloud-precipitation processes driving the evolution of this morphology regime (Figure 9). Aitken activation in the Cu layer generates accumulation aerosols that are grown by chemical processing throughout the BL and carried up to the drizzling Sc layer above by turbulent and convective motions. Simultaneously, eddies bring Aitken aerosols down to the Cu layer where they can be activated and grown. The continuous transfer of Aitken aerosol to the accumulation mode via activation in cloud droplets in the Cu and Sc layers buffers CCN against precipitation loss. Subsidence of Aitken aerosol from the free troposphere and generation at the surface were too slow to contribute significantly over these processing timescales of a few hours, but could be important in different BL cloud conditions. In particular, we estimate that BL Aitken concentrations can be restored between 0.1-6 days depending on their environment.

Aerosol sensitivity studies illustrate that Aitken buffering is essential in maintaining a thick homogeneous layer and preventing cloud break-up over the 12-hour duration of our simulation. Meteorological uplift enhances cloud moisture, and thus net cloud radiative effect, in this regime. In the absence of Aitken aerosols, this uplift would drive precipitation development and cloud break up. Precipitation-driven break up can be prevented if BL Aitken is present, even under halved accumulation concentrations. Even with the significant meteorological forcings present in the mid-latitudes, the processes driving cloud morphology evolution, heterogeneity, and radiative properties are sensitive to Aitken aerosols. Maintaining more reflective clouds for longer in this environment can be facilitated through Aitken buffering. Accounting for this influence in these pristine environments will be important for reducing aerosol-cloud interaction uncertainty in climate sensitivity.

Open Research

All of the ACE-ENA campaign observations are available at `https://www.arm.gov/research/campaigns/aaf2017ace-ena`. ECMWF ERA5 Reanalysis profiles associated with the campaign are available at `https://www.osti.gov/dataexplorer/biblio/dataset/1602289`. NASA SATCORPS VISST products for ARM are available at `https://www.arm.gov/capabilities/science-data-products/vaps/visst/xds` (ARM Data Center, 2017). Output from the simulations and scripts that can be used to reproduce the figures in the paper will be archived at Zenodo. The SAM model is publicly available at `http://rossby.msrc.sunysb.edu/~marat/SAM.html`. While the aerosol-enabled microphysics scheme used here is not included in the public release, it will be included in the Zenodo archive.

Acknowledgments

We thank all those who gathered, worked with, and provided data from the ACE-ENA field campaign and the accompanying satellite retrievals. Data were obtained from the Atmospheric Radiation Measurement (ARM) Program sponsored by the U.S. Department of Energy, Office of Science, Office of Biological and Environmental Research, Climate and Environmental Sciences Division. We acknowledge support from the U. S. Department of Energy Atmospheric System Research (DOE ASR) through grants DE-SC0020134 and DE-SC0021103. We also acknowledge the Extreme Science and Engineering Discovery Environment (XSEDE), which is supported by NSF grant number ACI-1548562, for enabling simulations performed on Bridges2 at the Pittsburgh Supercomputing Center through allocation EES210037. Research by ILM is supported by the NOAA Climate and Global Change Postdoctoral Fellowship Program, administered by UCAR's Cooperative Programs for the Advancement of Earth System Science (CPAESS) under award NA18NWS4620043B and by the NOAA cooperative agreements NA17OAR4320101 and NA22OAR4320151. CSB acknowledges support from the Allen Institute for AI. ILM thanks Amy, Daniel, and John McCoy for their insights and support. Finally, we thank Marat Khairoutdinov for developing, maintaining, and sharing SAM.

References

Albrecht, B. A. (1989, September). Aerosols, cloud microphysics, and fractional cloudiness. *Science*, *245*(4923), 1227–30. doi: 10.1126/science.245.4923.1227

ARM Data Center. (2017). Minnis Cloud Products Using Visst Algorithm (VISSTPX2DM10MINNIS). *Atmospheric Radiation Measurement (ARM) user facility, Eastern North Atlantic (ENA) External Data (satellites and others) (X1)*(2017-07-01 to 2017-07-31). (Data set accessed 2023-05-30)

Bellouin, N., Quaas, J., Gryspeerdt, E., Kinne, S., Stier, P., Watson-Parris, D., ... Stevens, B. (2020, March). Bounding Global Aerosol Radiative Forcing of Climate Change. *Rev Geophys*, *58*(1), e2019RG000660. doi: 10.1029/2019RG000660

Berner, A. H., Bretherton, C. S., Wood, R., & Muhlbauer, A. (2013). Marine boundary layer cloud regimes and POC formation in a CRM coupled to a bulk aerosol scheme. *Atmospheric Chemistry and Physics*, *13*(24), 12549–12572. doi: 10.5194/acp-13-12549-2013

Binkowski, F. S., & Shankar, U. (1995). The Regional Particulate Matter Model: 1. Model description and preliminary results. *Journal of Geophysical Research*, *100*(D12), 26191. Retrieved 2022-11-13, from `http://doi.wiley.com/10.1029/95JD02093` doi: 10.1029/95JD02093

Blossey, P. N., Bretherton, C. S., & Mohrmann, J. (2021, May). Simulating observed cloud transitions in the northeast Pacific during CSET. *Monthly Weather Review*. Retrieved 2022-09-10, from `https://journals.ametsoc.org/view/journals/mwre/aop/MWR-D-20-0328.1/MWR-D-20-0328.1.xml` doi: 10.1175/MWR-D-20-0328.1

Boucher, O. (2013). *Clouds and Aerosols* (Tech. Rep.). Cambridge University Press, Cambridge, United Kingdom and New York, NY, USA..

Bretherton, C. S., & Blossey, P. N. (2017). Understanding Mesoscale Aggregation of Shallow Cumulus Convection Using Large-Eddy Simulation. *Journal of Advances in Modeling Earth Systems*, *9*(8), 2798–2821. doi: 10.1002/2017ms000981

Bulatovic, I., Igel, A. L., Leck, C., Heintzenberg, J., Riipinen, I., & Ekman, A. M. L. (2021, March). The importance of Aitken mode aerosol particles for cloud sustenance in the summertime high Arctic – a simulation study supported by observational data. *Atmospheric Chemistry and Physics*, *21*(5), 3871–3897. Retrieved 2022-09-02, from `https://acp.copernicus.org/articles/21/3871/2021/` doi: 10.5194/acp-21-3871-2021

Carslaw, K. S., Lee, L. A., Reddington, C. L., Pringle, K. J., Rap, A., Forster, P. M., ... Pierce, J. R. (2013, November). Large contribution of natural aerosols to uncertainty in indirect forcing. *Nature*, *503*(7474), 67–71. doi: 10.1038/nature12674

Christensen, M. W., Gettelman, A., Cermak, J., Dagan, G., Diamond, M., Douglas, A., ... Yuan, T. (2022). Opportunistic experiments to constrain aerosol effective radiative forcing. *Atmospheric Chemistry and Physics*, *22*(1), 641–674. doi: 10.5194/acp-22-641-2022

Clarke, A. D., Varner, J. L., Eisele, F., Mauldin, R. L., Tanner, D., & Litchy, M. (1998, July). Particle production in the remote marine atmosphere: Cloud outflow and subsidence during ACE 1. *Journal of Geophysical Research: Atmospheres*, *103*(D13), 16397–16409. doi: 10.1029/97jd02987

Covert, D. S., Kapustin, V. N., Bates, T. S., & Quinn, P. K. (1996, March). Physical properties of marine boundary layer aerosol particles of the mid-Pacific in relation to sources and meteorological transport. *Journal of Geophysical Research: Atmospheres*, *101*(D3), 6919–6930. doi: 10.1029/95jd03068

Fan, J., Rosenfeld, D., Zhang, Y., Giangrande, S. E., Li, Z., Machado, L. A. T., ... de Souza, R. A. F. (2018, January). Substantial convection and precipitation enhancements by ultrafineaerosol particles. *Science*, *359*(6374), 411–418. Retrieved 2022-11-13, from `https://www.science.org/doi/10.1126/science.aan8461` doi: 10.1126/science.aan8461

Feingold, G., & Kreidenweis, S. M. (2002, December). Cloud processing of aerosol as modeled by a large eddy simulation with coupled microphysics and aqueous chemistry. *Journal of Geophysical Research: Atmospheres*, *107*(D23), AAC 6–1–AAC 6–15. Retrieved 2023-06-30, from `http://doi.wiley.com/10.1029/2002JD002054` doi: 10.1029/2002JD002054

Gordon, H., Kirkby, J., Baltensperger, U., Bianchi, F., Breitenlechner, M., Curtius, J., ... Carslaw, K. S. (2017, August). Causes and importance of new particle formation in the present-day and preindustrial atmospheres. *Journal of Geophysical Research: Atmospheres*, *122*(16), 8739–8760. doi: 10.1002/2017jd026844

Gordon, H., Sengupta, K., Rap, A., Duplissy, J., Frege, C., Williamson, C., ... Carslaw, K. S. (2016, October). Reduced anthropogenic aerosol radiative forcing caused by biogenic new particle formation. *Proceedings of the National Academy of Sciences*, *113*(43), 12053–12058. doi: 10.1073/pnas.1602360113

Heintzenberg, J., Covert, D. C., & Van Dingenen, R. (2000, September). Size distribution and chemical composition of marine aerosols: a compilation and review. *Tellus B*, *52*(4), 1104–1122. Retrieved 2022-12-30, from `http://www.tellusb.net/index.php/tellusb/article/view/17090` doi: 10.1034/j.1600-0889.2000.00136.x

Hoffmann, F., & Feingold, G. (2023, June). A Note on Aerosol Processing by Droplet Collision-Coalescence. *Geophysical Research Letters*, *50*(11), e2023GL103716. Retrieved 2023-06-30, from `https://agupubs.onlinelibrary.wiley.com/doi/10.1029/2023GL103716` doi: 10.1029/2023GL103716

Kaufman, Y. J., & Tanré, D. (1994, May). Effect of variations in super-saturation on the formation of cloud condensation nuclei. *Nature*, *369*(6475), 45–48. doi: 10.1038/369045a0

Kazil, J., Wang, H., Feingold, G., Clarke, A. D., Snider, J. R., & Bandy, A. R. (2011). Modeling chemical and aerosol processes in the transition from closed to open cells during VOCALS-REx. *Atmospheric Chemistry and Physics*, *11*(15), 7491–7514. doi: 10.5194/acp-11-7491-2011

Konsta, D., Dufresne, J., Chepfer, H., Vial, J., Koshiro, T., Kawai, H., ... Ogura, T. (2022, June). Low-Level Marine Tropical Clouds in Six CMIP6 Models Are Too Few, Too Bright but Also Too Compact and Too Homoge-

neous. *Geophysical Research Letters*, *49*(11). Retrieved 2022-06-04, from https://onlinelibrary.wiley.com/doi/10.1029/2021GL097593 doi: 10.1029/2021GL097593

Lawler, M. J., Saltzman, E. S., Karlsson, L., Zieger, P., Salter, M., Baccarini, A., ... Leck, C. (2021, November). New Insights Into the Composition and Origins of Ultrafine Aerosol in the Summertime High Arctic. *Geophysical Research Letters*, *48*(21). Retrieved 2022-09-21, from https://onlinelibrary.wiley.com/doi/10.1029/2021GL094395 doi: 10.1029/2021GL094395

Leahy, L. V., Wood, R., Charlson, R. J., Hostetler, C. A., Rogers, R. R., Vaughan, M. A., & Winker, D. M. (2012). On the nature and extent of optically thin marine low clouds. *Journal of Geophysical Research: Atmospheres*, *117*(D22), n/a–n/a. doi: 10.1029/2012JD017929

McCoy, I. L., Bretherton, C. S., Wood, R., Twohy, C. H., Gettelman, A., Bardeen, C. G., & Toohey, D. W. (2021, April). Influences of Recent Particle Formation on Southern Ocean Aerosol Variability and Low Cloud Properties. *Journal of Geophysical Research-Atmospheres*, *126*(8). doi: ARTNe2020JD03352910.1029/2020JD033529

McCoy, I. L., McCoy, D. T., Wood, R., Regayre, L., Watson-Parris, D., Grosvenor, D. P., ... Gordon, H. (2020, August). The hemispheric contrast in cloud microphysical properties constrains aerosol forcing. *Proceedings of the National Academy of Sciences*, *117*(32), 18998–19006. doi: 10.1073/pnas.1922502117

McCoy, I. L., McCoy, D. T., Wood, R., Zuidema, P., & Bender, F. A. (2023, January). The Role of Mesoscale Cloud Morphology in the Shortwave Cloud Feedback. *Geophysical Research Letters*, *50*(2). Retrieved 2023-02-01, from https://onlinelibrary.wiley.com/doi/10.1029/2022GL101042 doi: 10.1029/2022GL101042

Mieslinger, T., Stevens, B., Kölling, T., Brath, M., Wirth, M., & Buehler, S. A. (2021). Optically thin clouds in the trades. *Atmos. Chem. Phys. Discuss.*, *2021*, 1–33. doi: 10.5194/acp-2021-453

Minnis, P., Nguyen, L., Palikonda, R., Heck, P. W., Spangenberg, D. A., Doelling, D. R., ... Szedung, S.-M. (2008). Near-real time cloud retrievals from operational and research meteorological satellites. In R. H. Picard, A. Comeron, K. Schäfer, A. Amodeo, & M. v. Weele (Eds.), *Remote Sensing of Clouds and the Atmosphere XIII* (Vol. 7107, p. 710703). SPIE. Retrieved from https://doi.org/10.1117/12.800344 (Backup Publisher: International Society for Optics and Photonics) doi: 10.1117/12.800344

Minnis, P., Sun-Mack, S., Young, D. F., Heck, P. W., Garber, D. P., Chen, Y., ... Yang, P. (2011). CERES Edition-2 Cloud Property Retrievals Using TRMM VIRS and Terra and Aqua MODIS Data—Part I: Algorithms. *IEEE Transactions on Geoscience and Remote Sensing*, *49*(11), 4374–4400. doi: 10.1109/TGRS.2011.2144601

Morrison, H., Curry, J. A., & Khvorostyanov, V. I. (2005, June). A New Double-Moment Microphysics Parameterization for Application in Cloud and Climate Models. Part I: Description. *Journal of the Atmospheric Sciences*, *62*(6), 1665–1677. Retrieved 2023-07-05, from https://journals.ametsoc.org/doi/10.1175/JAS3446.1 doi: 10.1175/JAS3446.1

Narenpitak, P., Kazil, J., Yamaguchi, T., Quinn, P., & Feingold, G. (2021). From Sugar to Flowers: A Transition of Shallow Cumulus Organization During ATOMIC. *Journal of Advances in Modeling Earth Systems*, *13*(10). doi: 10.1029/2021ms002619

Neggers, R. A. J., Chylik, J., Egerer, U., Griesche, H., Schemann, V., Seifert, P., ... Macke, A. (2019, July). Local and Remote Controls on Arctic Mixed-Layer Evolution. *Journal of Advances in Modeling Earth Systems*, *11*(7), 2214–2237. Retrieved 2022-11-04, from https://onlinelibrary.wiley.com/doi/abs/

10.1029/2019MS001671 doi: 10.1029/2019MS001671

O, K.-T., Wood, R., & Bretherton, C. S. (2018, May). Ultraclean Layers and Optically Thin Clouds in the Stratocumulus-to-Cumulus Transition. Part II: Depletion of Cloud Droplets and Cloud Condensation Nuclei through Collision–Coalescence. *Journal of the Atmospheric Sciences*, *75*(5), 1653–1673. doi: 10.1175/jas-d-17-0218.1

O, K.-T., Wood, R., & Tseng, H.-H. (2018). Deeper, Precipitating PBLs Associated With Optically Thin Veil Clouds in the Sc-Cu Transition. *Geophysical Research Letters*, *45*(10), 5177–5184. doi: 10.1029/2018gl077084

Patrick Minnis, William L. Smith, Jr., David F. Young, L. Nguyen, Anita D. Rapp, Patrick W. Heck, ... Yan Chen (2001). A near-real time method for deriving cloud and radiation properties from satellites for weather and climate studies. *Proc. AMS 11th Conf. Satellite Meteorology and Oceanography*, *Madison, WI*(Oct. 15-18), 477–480. Retrieved from http://www-pm.larc.nasa.gov/arm_refs.html

Pöhlker, M. L., Zhang, M., Campos Braga, R., Krüger, O. O., Pöschl, U., & Ervens, B. (2021, August). Aitken mode particles as CCN in aerosol- and updraft-sensitive regimes of cloud droplet formation. *Atmospheric Chemistry and Physics*, *21*(15), 11723–11740. Retrieved 2022-09-18, from https://acp.copernicus.org/articles/21/11723/2021/ doi: 10.5194/acp-21-11723-2021

Rogers, R. R., & Yau, M. K. (1989). *A Short Course in Cloud Physics* (3rd ed.). Butterworth-Heinemann.

Sanchez, K. J., Chen, C. L., Russell, L. M., Betha, R., Liu, J., Price, D. J., ... Behrenfeld, M. J. (2018, February). Substantial Seasonal Contribution of Observed Biogenic Sulfate Particles to Cloud Condensation Nuclei. *Scientific Reports*, *8*(1), 3235. doi: 10.1038/s41598-018-21590-9

Seinfeld, J. H., & Pandis, S. N. (2016). *Atmospheric Chemistry and Physics : From Air Pollution to Climate Change*. New York, UNITED STATES: John Wiley & Sons, Incorporated.

Stevens, B., & Feingold, G. (2009, October). Untangling aerosol effects on clouds and precipitation in a buffered system. *Nature*, *461*(7264), 607–613. doi: 10.1038/nature08281

Tornow, F., Ackerman, A. S., Fridlind, A. M., Cairns, B., Crosbie, E. C., Kirschler, S., ... Sorooshian, A. (2022, June). Dilution of Boundary Layer Cloud Condensation Nucleus Concentrations by Free Tropospheric Entrainment During Marine Cold Air Outbreaks. *Geophysical Research Letters*, *49*(11). Retrieved 2022-11-05, from https://onlinelibrary.wiley.com/doi/10.1029/2022GL098444 doi: 10.1029/2022GL098444

Twohy, C. H., Clement, C. F., Gandrud, B. W., Weinheimer, A. J., Campos, T. L., Baumgardner, D., ... Tan, D. (2002, November). Deep convection as a source of new particles in the midlatitude upper troposphere. *Journal of Geophysical Research: Atmospheres*, *107*(D21), AAC 6–1–AAC 6–10. doi: 10.1029/2001jd000323

Twomey, S. (1959, May). The nuclei of natural cloud formation part II: The supersaturation in natural clouds and the variation of cloud droplet concentration. *Geofisica Pura e Applicata*, *43*(1), 243–249. Retrieved 2023-05-24, from http://link.springer.com/10.1007/BF01993560 doi: 10.1007/BF01993560

Twomey, S. (1977). The Influence of Pollution on the Shortwave Albedo of Clouds. *Journal of the Atmospheric Sciences*, *34*(7), 1149–1152. doi: 10.1175/1520-0469(1977)034⟨1149:Tiopot⟩2.0.Co;2

Wang, J., Wood, R., Jensen, M. P., Chiu, J. C., Liu, Y., Lamer, K., ... Zhang, Z. (2022). Aerosol and Cloud Experiments in the Eastern North Atlantic (ACE-ENA). *Bulletin of the American Meteorological Society*, *103*(2), E619–E641.

doi: 10.1175/bams-d-19-0220.1

Williamson, C. J., Kupc, A., Axisa, D., Bilsback, K. R., Bui, T., Campuzano-Jost, P., ... Brock, C. A. (2019, October). A large source of cloud condensation nuclei from new particle formation in the tropics. *Nature*, *574*(7778), 399–403. doi: 10.1038/s41586-019-1638-9

Wood, R. (2006). Rate of loss of cloud droplets by coalescence in warm clouds. *Journal of Geophysical Research: Atmospheres*, *111*(D21).

Wood, R., O, K.-T., Bretherton, C. S., Mohrmann, J., Albrecht, B. A., Zuidema, P., ... Minnis, P. (2018, May). Ultraclean Layers and Optically Thin Clouds in the Stratocumulus-to-Cumulus Transition. Part I: Observations. *Journal of the Atmospheric Sciences*, *75*(5), 1631–1652. doi: 10.1175/jas-d-17-0213.1

Wyant, M. C., Bretherton, C. S., Wood, R., Blossey, P. N., & McCoy, I. L. (2022, June). High Free-Tropospheric Aitken-Mode Aerosol Concentrations Buffer Cloud Droplet Concentrations in Large-Eddy Simulations of Precipitating Stratocumulus. *Journal of Advances in Modeling Earth Systems*, *14*(6). Retrieved 2022-06-25, from `https://onlinelibrary.wiley.com/doi/10.1029/2021MS002930` doi: 10.1029/2021MS002930

Xu, W., Ovadnevaite, J., Fossum, K. N., Lin, C., Huang, R.-J., Ceburnis, D., & O'Dowd, C. (2022, April). Sea spray as an obscured source for marine cloud nuclei. *Nature Geoscience*, *15*(4), 282–286. Retrieved 2022-06-08, from `https://www.nature.com/articles/s41561-022-00917-2` doi: 10.1038/s41561-022-00917-2

Zender, C. (2001). Particle Size Distributions: Theory and Application to Aerosols, Clouds, and Soils.

Zheng, G., Kuang, C., Uin, J., Watson, T., & Wang, J. (2020). Large contribution of organics to condensational growth and formation of cloud condensation nuclei (CCN) in the remote marine boundary layer. *Atmospheric Chemistry and Physics*, *20*(21), 12515–12525. doi: 10.5194/acp-20-12515-2020

Zheng, G., Wang, Y., Wood, R., Jensen, M. P., Kuang, C., McCoy, I. L., ... Wang, J. (2021, January). New particle formation in the remote marine boundary layer. *Nat Commun*, *12*(1), 527. doi: 10.1038/s41467-020-20773-1